arXiv:2411.11783v1 [cond-mat.mtrl-sci] 18 Nov 2024

Open Catalyst Experiments 2024 (OCx24): Bridging Experiments and Computational Models

Jehad Abed[1*], **Jiheon Kim**[2,5,6*], **Muhammed Shuaibi**[1*], **Brook Wander**[3*], **Boris Duijf**[7], **Suhas Mahesh**[4,6], **Hyeonseok Lee**[5,6], **Vahe Gharakhanyan**[1], **Sjoerd Hoogland**[2,6], **Erdem Irtem**[7], **Janice Lan**[1], **Niels Schouten**[7], **Anagha Usha Vijayakumar**[7], **Jason Hattrick-Simpers**[4,6], **John R. Kitchin**[3], **Zachary W. Ulissi**[1], **Aaike van Vugt**[7], **Edward H. Sargent**[2,6†], **David Sinton**[5,6†], **C. Lawrence Zitnick**[1†]

[1]Fundamental AI Research (FAIR) Meta, [2]Department of Electrical and Computer Engineering, University of Toronto, [3]Department of Chemical Engineering, Carnegie Mellon University, [4]Department of Material Science and Engineering, University of Toronto, [5]Department of Mechanical and Industrial Engineering, University of Toronto, [6]Alliance for AI-Accelerated Materials Discovery (A3MD), [7]VSParticle BV

The search for low-cost, durable, and effective catalysts is essential for green hydrogen production and CO_2 upcycling to help in the mitigation of climate change. Discovery of new catalysts is currently limited by the gap between what AI-accelerated computational models predict and what experimental studies produce. To make progress, large and diverse experimental datasets are needed that are reproducible and tested at industrially-relevant conditions. We address these needs by utilizing a comprehensive high-throughput characterization and experimental pipeline to create the Open Catalyst Experiments 2024 (OCx24) dataset. The dataset contains 572 samples synthesized using both wet and dry methods with X-ray fluorescence and X-ray diffraction characterization. We prepared 441 gas diffusion electrodes, including replicates, and evaluated them using zero-gap electrolysis for CO_2 reduction (CO_2RR) and hydrogen evolution reactions (HER) at current densities up to 300 mA/cm^2. To find correlations with experimental outcomes and to perform computational screens, DFT-verified adsorption energies for six adsorbates were calculated on ∼20,000 inorganic materials requiring 685 million AI-accelerated relaxations. Remarkably from this large set of materials, a data driven Sabatier volcano independently identified Pt as being a top candidate for HER without having any experimental measurements on Pt or Pt-alloy samples. We anticipate the availability of experimental data generated specifically for AI training, such as OCx24, will significantly improve the utility of computational models in selecting materials for experimental screening.

Date: November 18, 2024
Correspondence: E. H. Sargent (ted.sargent@northwestern.edu), D. Sinton (dave.sinton@utoronto.ca), C.L. Zitnick (zitnick@meta.com)
Code: https://github.com/FAIR-Chem/fairchem/tree/main/src/fairchem/applications/ocx, MIT license
Dataset: https://fair-chem.github.io/core/datasets/ocx24.html, Creative Commons 4.0 License

Meta

1 Introduction

The climate perturbations and ecological instability resulting from fossil fuel combustion and industrial processes necessitates a shift towards renewable and carbon-neutral energy solutions. The electrochemical Hydrogen Evolution Reaction (HER) holds the potential to generate green hydrogen from renewable energy for use in fuel cells, chemicals manufacturing, steel production and many other applications that could help abate CO_2 emissions[1]. The electrochemical CO_2 Reduction Reaction (CO_2RR) has emerged as an attractive method to transform our economy to one that is carbon-neutral through the recycling of CO_2[2]. This includes the opportunity to offset the costs associated with carbon capture by creating sustainable value streams for CO_2 utilization[2,3]. Currently, the deployment of HER and CO_2RR are limited in part due to the need to find durable and low-cost catalysts that can drive chemical reactions efficiently and selectively toward valuable products[3,4].

Catalyst discovery is a time consuming process of trial and error built on decades of expert domain knowledge[5–8]. Since the analysis of even a single material is time intensive, different areas of the material design space are typically evaluated in separate studies by independent institutions. As is well documented[9], the lack of reproducibility of these studies leads to challenges in building upon prior results, and hinders our ability to draw conclusions from the studies in aggregation[10,11].

Recently, the application of Artificial Intelligence (AI) to computational chemistry has dramatically increased the speed at which materials may be analyzed[12–16] as compared to traditional approaches using Density Functional Theory (DFT). Similar to other fields such as protein folding[17,18] and large language models[19,20], these ML approaches have improved significantly with large dataset initiatives including the Materials Project[21], Open Catalyst Project[22], OQMD[23,24], and others[25–28]. However, computational approaches typically rely on idealized structures and properties, which may not accurately represent the real-world lab conditions. Furthermore, typical experimental material performance properties, such as product selectivity, cannot be directly estimated from commonly calculated computational properties such as adsorption or transition-state energies.

How can we bridge the gap between computational models and experimental results? In this paper, we introduce Open Catalyst Experiments 2024 (OCx24), in which we perform experimental studies specifically designed to aid AI models in mapping computational properties to experimental results, Figure 1. To serve as effective training data, experimental studies must have several properties. The dataset should contain a diverse set of materials across the elemental space and cover both positive and negative results. Candidate samples should be evaluated in a reproducible manner and under industrially relevant conditions that may translate to large-scale reactors. Finally, the samples synthesized should be amenable to computational analysis. To accomplish this, we aim to study intermetallic nanoparticles[29], which are structurally ordered metal alloys with precise atomic stoichiometry. They are ideal for modeling catalysts computationally as a result of their well-defined structure. However, the experimental synthesis of these intermetallic nanoparticles is exceptionally challenging[30]. Synthesis conditions need to be carefully controlled to ensure the nanoparticles are of the appropriate size, single phase, and ordered[31]. Since high failure rates are common for synthesis, proper characterization is required for all samples to ensure they correspond to the target material.

For experimental screening, OCx24 utilizes two synthesis techniques, chemical reduction and spark ablation, to synthesize 572 samples covering a diverse set of samples of 13 different elements, as shown in Figure 2. To characterize each sample, X-ray fluorescence (XRF) and X-ray diffraction (XRD) were performed to determine its composition and to elucidate the purity and structure of the sample synthesized, respectively. Using this information, we filtered the samples to those that were single phase and had good structural matches to the desired compositional structures as determined by an automated XRD multiphase identification pipeline. Finally, electrochemical CO_2RR and HER testing were performed at industrially relevant current densities with priority given to samples that passed the prior filtering step. Without replicates, there were 230 unique sample preparations, but there are samples that have very similar compositions. After aggregating similar compositions, 179 experimental targets remained for downstream modeling efforts.

For computational screening, OCx24 calculates the adsorption energies of 6 adsorbate intermediates (OH, CO, CHO, C, COCOH, H) for 19,406 materials. We considered any material in the Materials Project (MP)[21], Open Quantum Materials Database (OQMD)[23,24], and Alexandria[32,33] that could be thermodynamically stable under reaction conditions (Pourbaix decomposition energy less than 0.05 eV/atom). Adsorption energy calculations were performed on surface terminations up to Miller index two using the AdsorbML pipeline[13] that combines AI and DFT calculations. This effort required 685 million structural relaxations and ∼20 million DFT single points and is the largest computational screening of catalysts for any application to date.

By combining the experimental and computational results, we built predictive models for HER. For this reaction, platinum catalysts are known to perform well, but their high cost limits their commercial deployment[4,34]. Models were trained to predict the cell voltage at 50 mA/cm^2 production rate using the adsorption energies of H and OH as features. A linear model was used to perform inference on the full set of 19,406 stable/metastable materials. In this high-data regime, we recover a Sabatier volcano with Pt predicted to be near the apex, despite there being no Pt-containing alloys in the training dataset. Through this analysis, we identify hundreds of potential HER catalysts, many of which are importantly composed of low-cost elements.

Finding a catalyst that outperforms copper for the production of multi-carbon products in CO_2RR remains

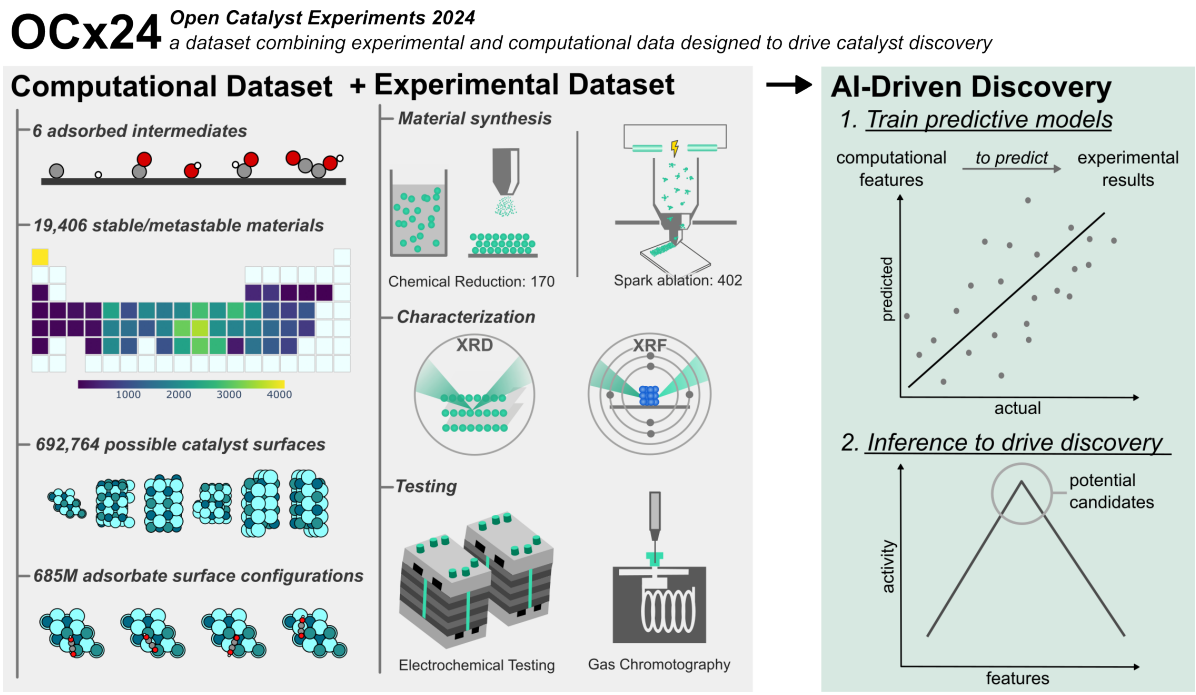

Figure 1 A summary of the computational and experimental screening efforts, and the resulting outcomes. Computationally, six adsorbates were used as descriptors and their adsorption energies were calculated across a wide swath of materials. Experimentally, two synthesis techniques were used to prepare 572 samples which were characterized and a subset tested. We used this data to build models capable of predicting experimental outcomes using computational features.

an outstanding challenge[35]. Despite copper's ability to produce multi-carbon products, improvements in activity, selectivity, and stability are desirable[2,35,36]. In our models, we predict CO_2RR production rates at a fixed applied potential to explore the selectivity of the catalyst. The correlation of the predictive models for H_2, CO, and liquid products is weaker than HER for this more complex reaction. Building predictive models is especially challenging when the model must generalize to novel compositions outside the training dataset. Further advances in modeling and additional training data offer promising future directions. Although this paper focuses on HER and CO_2RR, we expect these findings to be useful for many applications and chemistries beyond those studied here.

2 Experimental Methods

We determine the materials targeted for synthesis by sampling a diverse set of materials based on their elemental composition and a rough estimate of their expected products. For synthesis, we use two techniques to increase the diversity of the samples we use for testing, and to gain an understanding of the impact of different synthesis techniques. After characterization of the resulting samples using XRF and XRD, a subset of the samples is passed on for testing based in part on whether they match the target computational materials.

2.1 Synthesis Techniques

Diversity is essential when creating training data for ML models. When selecting materials to synthesize, this includes the diversity of their elemental composition and the diversity of the products produced when they are used as catalysts. To increase the likelihood of sampling materials that produce different products, we grouped the materials into three rough groups that are likely to produce hydrogen, C_1, and C_{2+} products and attempted to sample from them equally for synthesis. See Section A.1 for details on this process.

The synthesis of a diverse set of samples was the most significant challenge of this study. Given a desired

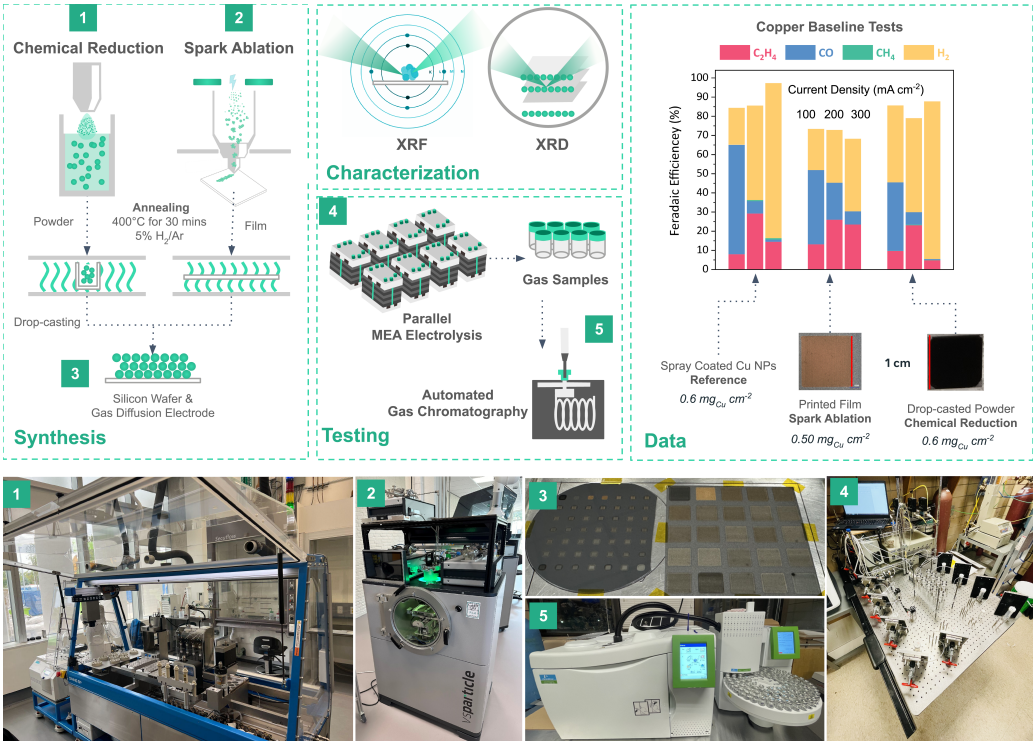

Figure 2 This figure illustrates the experimental pipeline, detailing the process from synthesis to characterization and testing. (right) Cu baselines for the two synthesis techniques and a reference technique using spray coated nanoparticles. Similar trends across current densities are seen for all techniques.

composition, a synthesis technique should ideally be capable of mixing metals in nanoparticles with controlled size and mass loading. This helps to eliminate the influence of structural variance between different synthesized samples on the local reaction environment (i.e. thickness, porosity, inhomogeneity). Another challenge in synthesis is that the alloys need to be deposited on a carbon gas diffusion layer (GDL) to facilitate gas reactions for catalyst testing. Attempts to use high-temperature synthesis methods, essential for alloying more than one metal, such as carbothermal shock synthesis[37] failed because the structure of the GDL was damaged during the process. Two synthesis techniques, chemical reduction and spark ablation, met our criteria and produced acceptable baseline results on Cu samples, see Figure 2 (right). We use both of these approaches to synthesize binary and ternary metal alloys in our study since they have complementary elemental accessibility, see Figure 3. Duplicate samples were synthesized in a subset of the experiments to aid in verifying the reproducibility of the sample synthesis and testing procedures.

Spark ablation is a dry method, which uses additive printing with electrical energy to fragment metal rods into nanoclusters under an inert gas that can be directly deposited on a GDL. This was accomplished using a VSParticle© nanoparticle generator (VSP-P1). The generator relies on a physical phenomenon similar to vaporization and condensation, which uses high-voltage sparks between two closely spaced metal or alloy rods to generate a localized plasma. The intense heat from the plasma vaporizes material from these rods (ablation), which then cools and condenses into nanoparticles. Using an impaction technique and a 3D printer, nanoparticles can be synthesized and printed in a few hours. After printing a sample on the GDL, it is annealed using a tube furnace at 400°C temperatures with reducing gas to target intermetallic alloyed nanoparticles. See Section A.2 for details on this process.

Chemical reduction was performed using an automated robotic system (Chemspeed) that performs wet chemistry operations. This approach uses metal salt precursors that are mixed and reduced using a reducing agent that donates electrons to the mixed metals. The resulting sample is then post-annealed at elevated temperatures to create alloyed nanoparticle powders. These powders are combined with a polymer binder and applied to a GDL via drop casting for testing. See Section A.3 for more details.

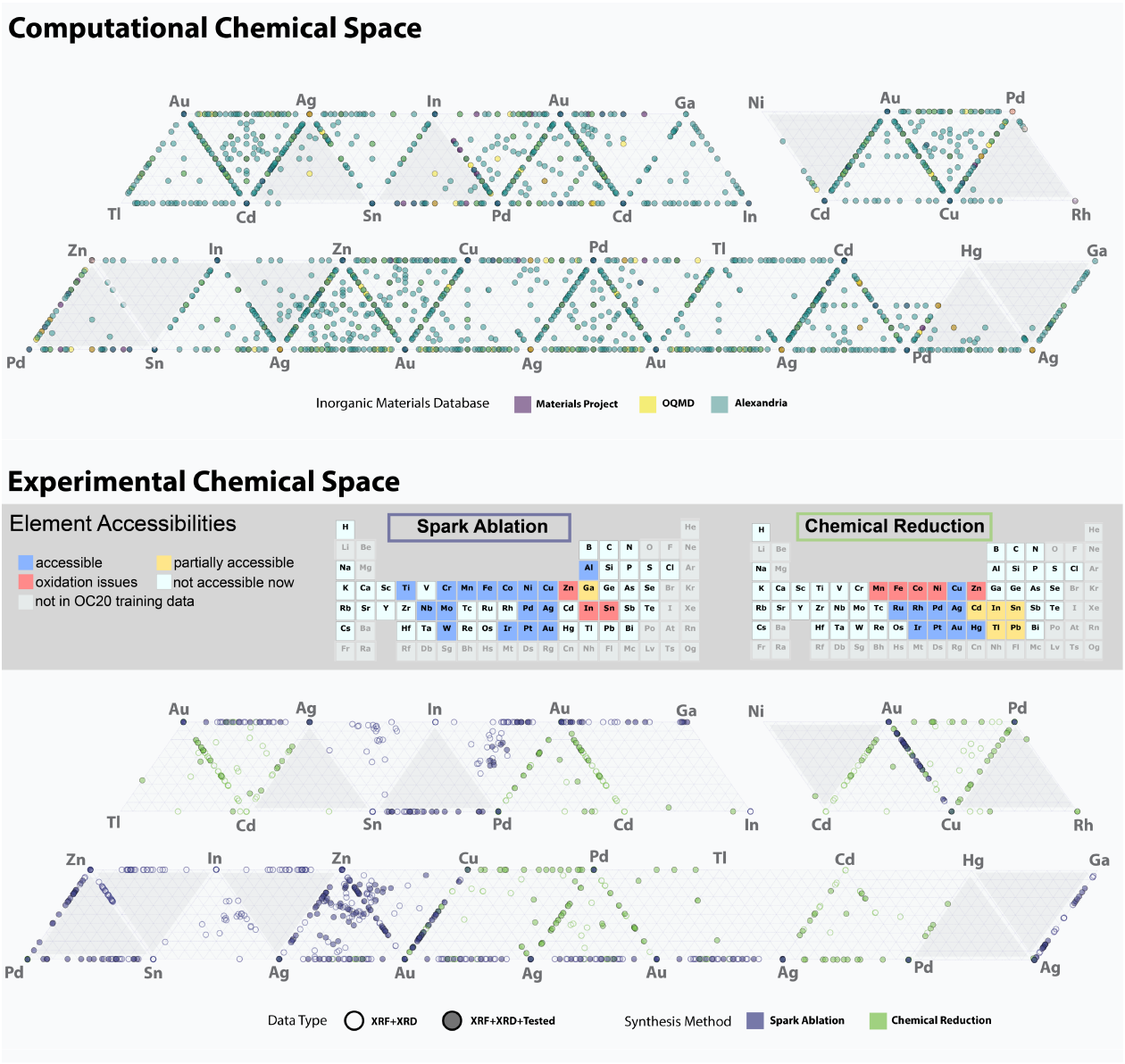

Figure 3 Chemical space anaylsis. (Top) Compositional diversity in the computational data considered for synthesis mapped and shown for each bulk database source: Materials Project (MP), Open Quantum Materials Database (OQMD), and Alexandria. (Bottom) Depiction of the accessibility of elements via the two synthesis methods (chemical reduction and spark ablation), along with a chemical space representation for all experimentally synthesized, characterized, and tested samples. Darker shaded ternary phase diagrams result from connecting several diagrams and were intentionally not explored.

2.2 Experimental Testing

Parallelized screening for CO_2RR and HER was performed using a modified membrane electrode assembly (MEA) setup from a previous study[38]. The testing process began with the electrolyzer operating at 50 mA/cm^2 for 9 minutes to evaluate HER activity. Afterward, CO_2 gas was introduced (flow rate: 30 s.c.c.m.) into the electrolyzers, and the CO_2RR was carried out at current densities of 50, 100, 150, 200, and 300 mA/cm^2 for 9 minutes each. The gas products were collected into headspace vials during each step of the CO_2RR process and subsequently analyzed using gas chromatography (PerkinElmer Clarus 590) with an autosampler (PerkinElmer TurboMatrix HS110). The gas products were detected by a thermal conductivity detector (TCD) and a flame ionization detector (FID) using high-purity Ar (99.999%) as the carrier gas. For further details, see Section A.4.

For the experimental results of HER, we recorded the full cell voltage of the MEA. Using a three-electrode MEA cell setup, we measured voltage losses across each component—membrane, anode, and internal resistance (IR) losses to identify voltage losses. This method, validated in a previous study[39] with the same type of MEA cells used in this work, allowed us to estimate the cathodic half-cell potential relative to the standard hydrogen electrode (SHE) (see Figure 13. Ideally for CO_2RR we would record production rates for different products at a fixed voltage. However, our studies used five fixed current densities. To account for this, we use logarithmic linear interpolation to estimate results for a fixed voltage, see Section C.3. The liquid product Faraday efficiency was estimated by subtracting the total percentage of the gaseous product from 100%.

3 Characterization Methods

3.1 Composition and Structure Validation

After synthesis, characterization is needed to verify whether the sample produced matches the target material. Precise verification of the target material is challenging and difficult to perform at high throughput[40]. In our study, we use two techniques: X-ray fluorescence (XRF) and X-ray diffraction (XRD). XRF measures the composition of the sample, that is, the percentage of elements in the sample. XRD provides insights into the fraction of material phases existing in the sample and the crystal structure of each phase. It is important to note that a sample that matches both XRF and XRD measurements does not guarantee that it is the same as the target material, since both measurements possess inherent limitations. XRF provides elemental analysis without specifying chemical forms, while XRD may encounter challenges with similar crystal structures, complex phases, and low crystallinity. Although integrating XRF and XRD enhances material identification, ambiguities and detection limits persist, which necessitates careful interpretation and potentially supplementary methods. However, they are effective in finding true negatives and samples that contain multiple phases. All characterization measurements were performed on samples deposited on silicon wafers to avoid an interference XRD signal from the underlying GDL substrate. For the spark ablation synthesis, the GDL and silicon wafer samples were printed at the same time, one layer at a time, to ensure the samples closely matched. See Section B for XRF and XRD details.

3.2 XRD Analysis

To conduct XRD analysis and identify phase combinations in samples, we developed an automated tool that streamlines the matching and refinement process. This tool compares experimental XRD pattern, i.e., peak position and intensity array, with computational XRD patterns that are generated from structures in the Materials Project, OQMD, and Alexandria, as well as experimental references from the Crystallography Open Database (COD)[41]. The process is conducted in four steps:

- Similarity Analysis (Figure 10): We start by matching the position and intensity of experimental XRD pattern with simulated patterns from computational structures.
- Multiphase matching (Figure 11): Once a phase is matched, we remove it from the experimental XRD pattern. We then repeat the first step to find additional phases. This process continues until all phases are identified or a user-defined limit is reached.

- Matching goodness evaluation (Figure 12): Finally, we refine the XRD fit using Rietveld refinement[42,43]. This step checks how well the identified phases match the experimental data. A quick and rough Rietveld fitting helps us assess the quality of the match by calculating the weighted profile R score (R_{wp}), which evaluates the fit's quality (the lower, the better). We report fits that are below an R_{wp} threshold of 50, as larger values typically indicate poor-quality fits that do not provide additional value to our analysis.

To find the best crystal structure match to the synthesized sample, we look for XRD matching solutions (phase mixtures) containing one phase that meet the following two conditions:

- The major phase has a weight fraction more than 70 wt.% of the phase mixture.
- The composition (atomic fraction) in the matched phase is close to what we measured in the sample using XRF (within ± two standard deviations). We determine the standard deviation by measuring the XRF composition at three different spots on the sample.

We then rank the phases that meet the above criteria based on the refinement R_{wp} score. We consider the phase to be a potential match using a score we call q, which is calculated as follows:

$$q_i = 100 \cdot \exp(-\alpha \cdot (R_{wp,i} - R_{wp,min})) \tag{1}$$

In this equation, α is a constant scaling factor set to 0.05. $R_{wp,i}$ is the R_{wp} value of the phase being considered and $R_{wp,min}$ is the lowest R_{wp} value (best fit) across all of the phases considered as potential possibilities to match the measured XRD spectrum. The q-score is used to assess the goodness of fit relative to other possible solutions. In this work, we designate samples as matched if they have a phase with weight fraction $\geq$70 wt.%, $q_i \geq 70$ and an $R_{wp} \leq 40$. See Section B for more details.

4 Computational Methods

Our goal is to develop computational models capable of mapping a set of descriptors for a material to their observed experimental performance over a broad range of materials. Other attempts at computational modeling use experimental data mined from literature[44–46], which is significantly more challenging since the materials may be synthesized and tested under varying conditions, unlike this study. Using results from single lab studies simplifies the problem. Without consistent testing conditions, experimental conditions along with elemental features have been used as inputs to ML models for guiding the selection of performant materials[47–49].

In our study, we explore the use of *ab initio* features in predicting experimental outcomes. *Ab initio* features have been shown to be predictive of catalyst trends[50–52] and are used to computationally screen material spaces[53–58]. There are only a few examples where screening is successfully used to identify catalyst candidates that are experimentally performant[59,60]. OCx24 goes beyond what has previously been performed by focusing on material diversity and their performance in complex reactions like CO_2RR.

4.1 Computational Material Selection

As inputs to our computational models, we consider all materials available in three permissively licensed computational materials databases: MP[21], OQMD[23,24], and Alexandria[32,33]. These datasets cover a much wider range of materials than our experimental dataset and may be useful in guiding future material exploration. In an effort to improve the likelihood of discovering an industrially viable catalyst, we filtered materials by assessing their thermodynamic stability under reaction conditions. To do this, we evaluate the decomposition energy using the Pourbaix framework implemented in pymatgen[61–63], see Section C.1 for details. This results in 19,406 total materials after deduplication (2,458 materials from MP, 3,173 materials from OQMD, and 13,775 materials from Alexandria) for use in our computational pipeline.

4.2 Descriptor Selection

Ab initio features based on adsorption energies, which estimate the attraction of different intermediate molecules to the surface of a catalyst, are commonly used as descriptors. Bagger et al.[64] calculated the

adsorption energies of five intermediates (H, CO, COOH, CH_3O and HCOO) for 16 unary materials with known product preferences to determine which descriptors provide separability of products in the descriptor space. They recommend using H, COOH, CO and an adsorbate with oxygen binding character to gain full separability. Peng et al.[65] show that monoatomic carbon is an important intermediate for the production of multi-carbon products and use C and CO to make a selectivity map to search for alloy candidates. Liu et al.[66] make a selectivity heatmap using CO and the H-CO transition state as descriptor energies. Later, Zhong et al.[60] demonstrated that the same character could be retained using H and CO adsorbates.

We selected our list of adsorbates (C, H, CO, OH, CHO, and COCOH) to include the characteristics and descriptors identified in these prior works with the objective of designing universal predictive models. In addition to the simple adsorbates, CHO and COCOH mark key points in the reaction network to produce non-formate C_1 and C_{2+} products[2], while OH offers orthogonal information since oxygen species generally do not scale linearly with hydrogen and carbon. All adsorbates are shown in Figure 1. For each adsorbate, the adsorption energy is calculated using the hybrid ML and DFT AdsorbML[13] pipeline for all Miller indices up to two for the entire dataset of 19,406 materials. These calculations required more than 685 million structural relaxations and ∼20 million DFT single points and is the largest computational screening of catalysts for any application to date. See Section C.2 for additional details.

In addition to *ab initio* features, we also consider descriptors for bulk material properties using Matminer[67]. In particular, we included the material Mendeleev number, row number, group number, atomic mass, atomic radius, and Pauling electronegativity. This includes characteristics that do not have an obvious relationship to catalytic properties.

4.3 Predictive Models

Catalyst performance for nanoparticles is an aggregate property over many surfaces, which may or may not be catalytically active. A predictive model may combine surface-level descriptors (e.g., adsorption energies) with bulk material properties (e.g., Matminer features) to estimate the experimental performance of the aggregated material. It is clear how material-level properties can be leveraged to predict other material-level properties, but aggregating surface-level properties to predict material-level properties is more challenging. This is in part due to the fact that the estimation of which surfaces will be realized experimentally is a difficult[68,69] and open problem. We explore three approaches to combining surface-level descriptors. First, we consider the simplest case - using the mean adsorption energy across all surfaces:

$$E_{ads,mean} = \frac{1}{N}\sum_{i}^{N} E_{ads,i} \tag{2}$$

where i iterates over the N surfaces and $E_{ads,i}$ is the surface's adsorption energy. The second uses Boltzmann weighting for both the adsorption energies and the surface energies given the set of surfaces using:

$$E_{ads,Boltz.} = \frac{\sum_i^N E_{ads,i} e^{-(E_{ads,i}-E_{ads,min})/(k_bT)} e^{-(E_{cl,i}-E_{cl,min})/(k_bT)}}{\sum_i^N e^{-(E_{ads,i}-E_{ads,min})/(k_bT)} e^{-(E_{cl,i}-E_{cl,min})/(k_bT)}} \tag{3}$$

where $E_{cl,i}$ is the cleavage energy on that surface and $E_{ads,min}$ is the material's minimum adsorption energy and similarly for $E_{cl,min}$. This results in surfaces with lower energies, which are more likely to be realized in practice, having higher weight. It also results in lower, more favorable adsorption energies having higher weight. The third approach uses the Wulff construction[70], which is a minimization of the total energy over a nanoparticle as a function of the surface energies of the various possible terminations with different geometric character[71]. For non-unary materials, it can be difficult to calculate surface energies, but the cleavage energy may be used as a proxy. Wulff constructions were performed using pymatgen[62,72]. Given a subset of $M \subset N$ surfaces appearing on the Wulff shape for a material with facet fractions $w_i, i \in M$ ($\sum_i w_i = 1$), we calculate the Wulff weighted energies using:

$$E_{ads,Wulff} = \sum_{i}^{M} w_i E_{ads,i} \tag{4}$$

Finally, the experimental values x are predicted using:

$$x = f(E_{ads,X}, b) \tag{5}$$

where f is a function learned from the experimental training data, and $E_{ads,X}$ is one of the aggregated adsorption energies (mean, Boltz., Wulff), and b are the bulk descriptors (e.g., Matminer features). When cleavage energies were not available (convergence errors, etc.) to compute Wulff and Boltzmann weighted energies, mean energies were used. All features were standardized to unit variance before training.

We employ two regression models that will be presented here: a simple linear regression model and a random forest regression model. Besides these models, we also explored Gaussian process, kernel ridge, support vector regression, and gradient boosting regression models; all use the implementation in scikit-learn [73,74] and xgboost [75] Python packages.

5 Results

For our results, we explore whether models trained on experimental data using computational descriptors as input can produce results that are predictive of held out experimental data. Given the chemical diversity of the data, and the complexity of reactions like CO_2RR, we are mainly looking at whether the models can predict trends and we are not focused on the absolute accuracy of the results. In many applications, the ability to rank candidates for a particular reaction is itself an impactful contribution. It is our hope that this study will provide the basis for future research in further understanding the connections between computational models and experimental studies.

For each model, we evaluate its performance under two different cross validation (CV) strategies:

> **Leave One Out (LOO)**: Hold out a given sample, train on the remaining data, and evaluate on the held out sample.
>
> **Leave One Composition Out (LOCO)**: Hold out all samples with a given composition (i.e. all Au_xCu_y samples, where x,y > 0), train on the remaining data, and evaluate on all held out samples.

A high correlation for LOO indicates the model can predict outcomes for samples that share compositions with those in the training dataset, while a high LOCO correlation indicates the model can generalize to novel compositions. LOCO presents a more difficult task for the model, removing the ability to interpolate between samples of similar composition.

The dataset contains samples that are matched and unmatched to an exact crystallographic structure (see Figure 15 for XRD analysis results). Matching was performed using the characterization data from XRD and XRF. When a match was available, we aggregated adsorption energies from only the corresponding matched bulk. Otherwise, we aggregated across the bulk material or materials with a composition closest to that of the XRF composition. Of the 441 electrochemical tests performed, 230 were intended to be distinct sample preparations. Among the 230, there were samples with compositions that were very close to each other. We averaged over these samples to obtain 179 experimental targets for modeling efforts, 43 of which were matched (Phases with a fraction $\geq$70 wt.%, R_{wp} score $\leq$40 and q-score $\geq$70%). We found that training jointly on matched and unmatched samples, outperforms just training on matched alone (Figure 21). The complete set of tabulated results for our best performing HER and CO_2RR models are provided in Table 2.

There are several nuances to handling the data that are worth noting. In some cases, samples labeled as matched have similar stoichiometries and match to the same bulk material. In this case, the sample with the composition closest to its matched bulk composition was retained and others discarded. For unmatched samples, if multiple samples correspond to the same bulk material based on XRF, the experimental results were averaged across all samples with the same synthesis technique. Lastly, if any sample in a group of replicates contained an XRD match, the result is also considered a match. Across replicates, we computed the mean experimental measured quantities. Alternative methods to aggregating experimental samples may be explored for downstream predictive tasks.

5.1 Hydrogen Evolution Reaction (HER)

The results of training models to predict the experimental voltage for HER is shown in Figure 4. Results are shown for a linear model trained on (top) H and OH adsorption energies as features and (bottom) Matminer features. Additional results can be found in Section C.4.1. A parity plot between the predicted voltage and

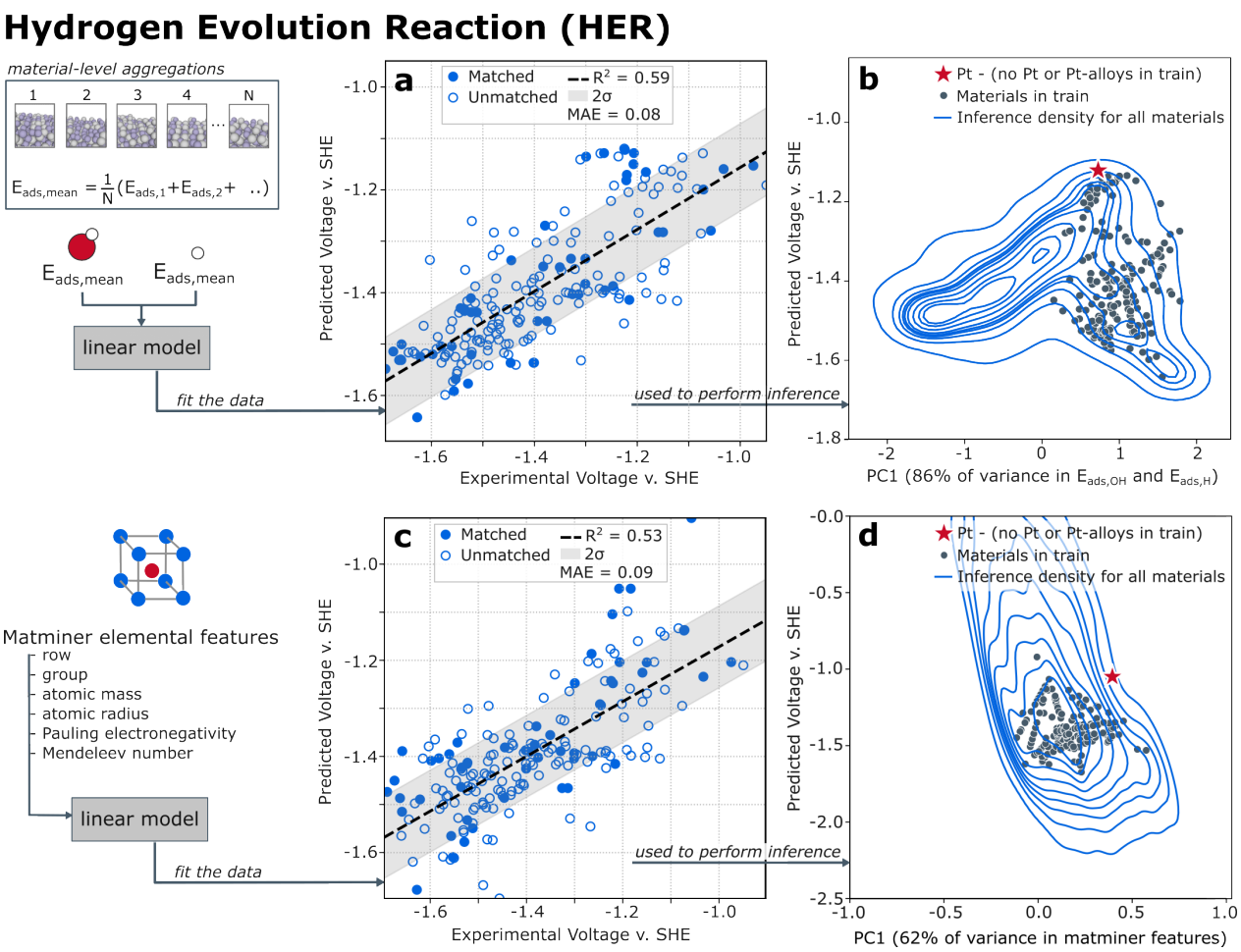

Figure 4 A summary of the inference campaign using models fit on hybrid data with (top) mean OH and H energies as features and (bottom) using Matminer features. A simple, linear model was trained with LOCO CV to obtain the predictive models (a and c). Using this fit and the computational descriptors for all stable/metastable materials assessed, we performed inference (b and d). The model trained on Matminer features does not generalize well (d), but the model trained on adsorption energies reveals a data driven Sabatier plot (b). Pt, which is annotated at the top of the volcano, was completely absent from the training data - even as an alloy.

experimental voltage using LOCO cross validation is shown in Figure 4a and 4c. The predictions and actual values are fairly well-correlated for both feature sets with $R^2 = 0.59$ for adsorption energies and $R^2 = 0.53$ for Matminer features. The trendline for the correlation is shown in Fig. 4a and 4c as a black dashed line. There was a modest performance improvement ($R^2 = 0.61$) by including all adsorption energies rather than just OH and H, but this result is not shown here for simplicity. On average, we observe an experimental standard deviation of $\sigma = 0.043$V vs SHE for 297 sample replicates within $\pm 5\%$ in XRF composition, an estimate of the noise in our targets (shaded gray in Figure 4).

Using these linear models, we performed inference across all 19,406 stable and metastable materials included in the computational workflow, which is shown in Fig. 4b and 4d. A simple principal component analysis (PCA) was performed to collapse the features into a single dimension (x-axis) for the purposes of visualization. The principal component found explains 86% of the variance for the adsorption energy features and 62% for the Matminer features. The y-axis (predicted voltage v. SHE) should be taken to be a reflection of the material activity, with more positive values being more desirable. The samples appearing in train are annotated individually as points on the plot. Platinum, which does not appear in the training data and is well known as an effective catalyst for HER, is annotated by a red star. The inference data is represented as a density contour plot using kernel density information since the number of materials considered is so large.

In this high-density data regime, we recover a Sabatier volcano for the model trained on mean OH and H adsorption energies, with platinum sitting at its peak despite platinum not appearing in the training data even as an alloy. Platinum is accessible by both of our synthesis methods, but platinum-containing materials were not selected as a part of our material selection process in part because of random chance.

Despite the models trained on Matminer[67] features achieving similar correlations to those trained on adsorption energies, when using Matminer features for inference we do not predict platinum to be an apex catalyst as shown in Figure 4d. In fact, roughly half of all materials assessed are predicted to be more active than platinum (less negative voltage v. SHE). This is likely because the adsorption energies are more generalizable, underscoring their usefulness.

There are 3,869 materials that are predicted to have a voltage within twice the mean absolute error (MAE) of Pt or better. A complete list of the 3,869 materials has been included with the datasets. Among the materials predicted to be good HER catalysts, there are 19 Mo-S, Mo-Se, and Mo-Se-S alloys. This aligns well with experimental precedent that these materials are good HER catalysts[76–79]. There are also 2,447 materials that contain Pd and / or Pt. This is not surprising since unary Pt and Pd are high-performing elemental catalysts for HER[80,81]. Still, there are 436 materials that do not contain Pd, Pt, Rh, Ir, Ru, Au, Os, or Ag which are potential low-cost HER catalysts. Among these, 282 are Se containing. The 200 best potential low-cost catalysts have been included in a table in the supplementary information, Section C.5.

The correlation between experimental results and computation descriptors improves with training dataset size, as explored in Figure 6. From this analysis we project that increasing the dataset size to 10^4 or 10^5 will allow for significantly more predictive models to be built.

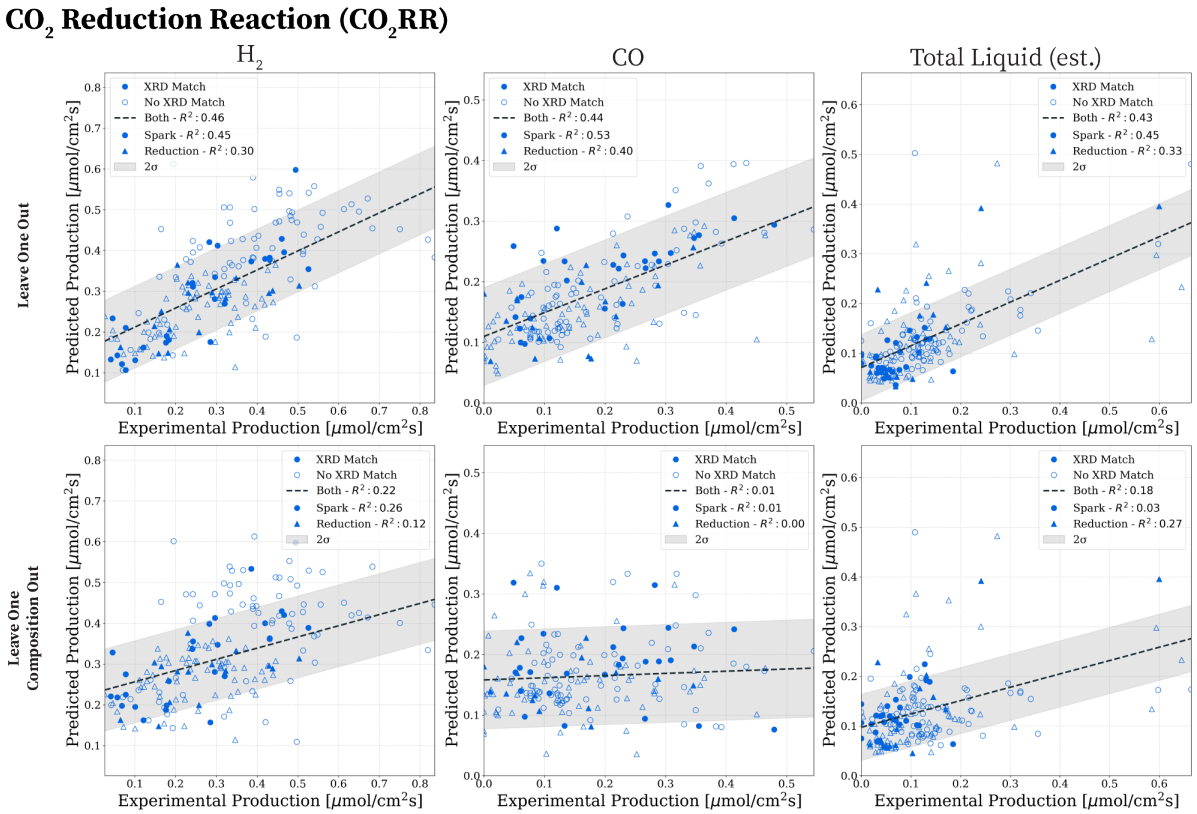

Figure 5 A summary of the CO_2RR predicted production rates across several products - H_2, CO, and Total Liquid (estimated) for the two different cross-validation strategies. Results showcase the complexity when trying to predict on unseen compositions (LOCO - bottom). A random forest regression model was used with features coming from Boltzmann weighted adsorption energies and elemental Matminer features. The shaded region corresponds to twice the average standard deviation in the experimental targets for samples within ±5% XRF composition.

	R^2			
	HER		CO_2RR	
Features	LOO	LOCO	LOO	LOCO
$E_{ads,mean}$	0.61	**0.59**	0.29	0.05
$E_{ads,Wulff}$	0.44	0.41	0.03	0.00
$E_{ads,Boltz.}$	0.26	0.21	0.10	0.00
Matminer-only	0.58	0.52	0.39	0.10
$E_{ads,mean}$ + Matminer	**0.63**	**0.59**	**0.46**	0.21
$E_{ads,Wulff}$ + Matminer	0.59	0.54	0.34	0.16
$E_{ads,Boltz.}$ + Matminer	0.59	0.54	**0.46**	**0.22**

Table 1 Feature analysis on HER and CO_2RR for their predictive performance. Results evaluated under both cross-validation strategies - LOO and LOCO. H_2 was used for CO_2RR correlations. Adsorption energy features have a strong correlation for HER but little to no correlation for CO_2RR.

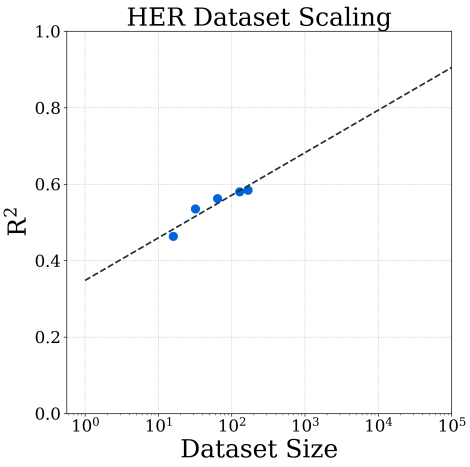

Figure 6 HER correlation results as a function of dataset size evaluated using LOCO cross-validation.

5.2 CO_2 Reduction Reaction (CO_2RR)

To evaluate our predictive models for CO_2RR, we first address a few notable experimental differences to HER. While HER has only one measurable outcome, the experimental voltage, CO_2RR has many possible products including CO, H_2, CH_4, C_2H_4, and liquid products. For a given experimental sample, CO_2RR testing was performed on each sample at several different current densities. To train a single model across the different compositions, we normalize the kinetic driving force, or potential, of the reaction. Given our experimental setup aimed to mirror industrial relevant conditions with two electrodes, fixing the potential through a three-electrode measurement was out of scope. To address this, we interpolate each product to a fixed applied potential of 3.3 V full cell voltage, the average potential across all testing experiments (see Section C.3 and Figure 14). This was performed for each sample and the interpolated results were used as targets for the regression models.

For each product, we independently fit a random forest regressor to predict the production rate. We directly measured the quantites of H_2, CO, CH_4, and C_2H_4 using gas chromatography. We attempted to fit models for each of these products and also Total Liquid (est.), which is the balance over electrons assuming that the remaining product is formate (two electrons transferred). Boltzmann weighted adsorption energies and Matminer elemental features were used as inputs. The results are shown in Figure 5 for a few products under different cross-validation strategies. When evaluating LOO performance, we capture fair correlations for H_2 ($R^2 = 0.46$), CO ($R^2 = 0.44$), and the liquid products ($R^2 = 0.43$). In general, results using spark ablation (circle markers) have stronger correlation than those using chemical reduction (triangle markers). However, results using LOCO suggest little correlation for H_2 ($R^2 = 0.22$), and the liquid products ($R^2 = 0.18$) and no correlation for CO ($R^2 = 0$). The results for C_2H_4 are similarly poor, with $R^2 = 0.08$ and 0.01 on LOO and LOCO, respectively. To predict the noise in our experimental results, we compute the standard deviation from 297 testing replicates within ±5% in XRF composition. We observe an experimental standard deviation of $\sigma = 0.050$ (H_2), 0.040 (CO), 0.033 (Liquid) μ mol/cm^{2}s as shown by the shaded areas in Figure 5.

Rather than fitting on production rates, we also explored fitting directly on the Faradaic efficiencies for each product, with similar results (Figure 22). When considering only the elemental features from Matminer, results are comparable to those when considering adsorption energies (Figure 20). This is a good indicator that there exists a large gap between the simple adsorption energies and the reality of CO_2RR. Additional results are highlighted in Section C.4; each with similar performance to those highlighted here.

Unlike HER, CO_2RR presents significant obstacles in building experimentally predictive models. These results suggest that leveraging only elemental features and adsorption energies of lone adsorbates on clean surfaces is not sufficient to predict the complexity of this chemistry. Despite these results, we hope they, alongside the

experimental dataset, provide an initial baseline for the community to evaluate more sophisticated predictive models.

5.3 Descriptor Importance

For both CO_2RR and HER we compare their performance using different adsorption energy and elemental features to predict H_2 and Voltage, respectively. We focus on H_2 for CO_2RR due to the weak signals for the other products. The importance of features is evaluated for both LOO and LOCO. A linear model is used for HER and a random forest model for CO_2RR, giving their respective best results. Results are summarized in Table 1.

For HER we see fairly consistent results across the board, with $R^2 \sim 0.6$ for all LOO results, with the exception of the Boltzmann and Wulff weighting ($R^2 = 0.26$ and 0.44, respectively). The naive $E_{ads,mean}$ performs the best on LOCO with a $R^2 = 0.59$ and LOO with the addition of Matminer features of $R^2 = 0.63$. CO_2RR results follow different trends. We observe that using only adsorption energy features provides the worst results on both LOO and LOCO, $R^2 \sim 0.3$ and $R^2 \sim 0$, respectively. Only with the inclusion of Matminer features does a weak correlation appear with $R^2 \sim 0.46$ and $R^2 \sim 0.22$ for LOO and LOCO, respectively. These results suggest that for HER the proposed adsorption energy descriptors are in fact beneficial and correlate well to experiments. In the case of CO_2RR, however, these descriptors have almost no correlation, specifically when looking at LOCO.

The Wulff shape can provide the theoretical, equilibrium nanoparticle structure of a material and the frequency of specific surfaces[70,72]. Unfortunately, we did not see clear improvements with all methodologies when using Wulff or Boltzman weighting over taking the simple mean of the adsorption energies. This shows a need to construct different methods of aggregating surface information to the material property level. We also saw no improvement when considering a single characteristic surface (the closed-packed surface in our case) as is done for small screening studies[66,82,83] which develop activity or selectivity projections as a function of 1-2 descriptors.

6 Conclusion

In this work, we strive to bridge the gap between computational models and experimental studies. While datasets for building computational ML models have grown substantially[22,25–28], constructing larger datasets of experimental results has proven challenging. This severely limits our ability to train models that map computational descriptors to experimental results. To address this, we perform a high-throughput experimental study at industrially relevant conditions for HER and CO_2RR covering 441 catalyst samples. Each sample was tested in a consistent manner and characterized by XRD and XRF to facilitate their connections to computational descriptors. In addition to a large experimental dataset, we present the largest computational catalyst screening campaign to date. It leverages machine learning to consider a previously intractable material design space of 19,406 materials. For each material, we calculated the adsorption energies of six adsorbates, including a multicarbon adsorbate, on all surfaces up to Miller index 2 with DFT validation.

The simulations for this study neglect several intricacies, which have been shown to have notable impacts on a catalyst's activity. The electrolyte, pH, gas-solid-liquid interface, temperature, and reactor design all have an impact on performance[2,84]. These findings extend to the computational realm as well. Theoretical work has shown that electric field effects at the surface stabilize important intermediates[85,86]. In a related manner, the pH and electrolyte have also been shown to impact product selectivity and activity[87,88]. Lastly, inclusion of solvent in simulations and the solvent approach can have a large impact on the resultant selectivity and/or activity[89,90].

Despite our simplifications, we were able to develop a strong correlation between HER experimental results and computational adsorption energies (H and OH). Using the correlation, we were able to predict the experimental activity of the 19,406 materials considered in the computational pipeline. This reveals a Sabatier volcano on which Pt is a top catalyst, despite the fact that Pt and Pt-alloys are absent from the training data. A list of materials are provided that are predicted to be more active than platinum.

Correlations for CO_2RR using adsorption energies from six adsorbates are weaker and demonstrate the challenges and opportunities for future research in predicting the selectivity of complex reactions. In addition to the complexity of electrochemical conditions, CO_2RR is difficult to treat because of its reaction network complexity. Producing a product selectively is a grand challenge because there are many competing possible products, chief among them being hydrogen gas[2]. Even when only considering products with up to two carbons, there are hundreds of possible reactions to make those products. There is no clear consensus on which reaction pathways are important for just pure copper[2,65,91], and even less clarity on which pathways are important for an arbitrary material.

There is opportunity to improve the work presented here, in an effort to realize AI-driven discovery for CO_2RR, by constructing a larger experimental dataset. As shown for HER in Figure 6, the addition of more data results in improved correlations. More data would also allow the possibility of using more complex modeling techniques that may better fit CO_2RR data. In addition, the impact of neglecting electrochemical conditions in the computational pipeline should be considered. Perhaps considering the network explicitly would improve our ability to make connections. This could be tractable since machine learning potentials (MLP) can be used to rapidly access transition state information[14]. There is also opportunity to explore different modeling techniques and in particular how to perform the abstraction from computational surface-level properties to aggregated material-level production rates. This problem is difficult, but important. Hopefully the creation of this dataset and datasets like it in the future will allow computationally driven experimental discovery to become a reality.

References

[1] MG Rasul, MA Hazrat, MA Sattar, MI Jahirul, and MJ Shearer. The future of hydrogen: Challenges on production, storage and applications. *Energy Conversion and Management*, 272:116326, 2022.

[2] Stephanie Nitopi, Erlend Bertheussen, Soren B Scott, Xinyan Liu, Albert K Engstfeld, Sebastian Horch, Brian Seger, Ifan EL Stephens, Karen Chan, Christopher Hahn, et al. Progress and perspectives of electrochemical CO_2 reduction on copper in aqueous electrolyte. *Chemical reviews*, 119(12):7610–7672, 2019.

[3] Wilson A Smith, Thomas Burdyny, David A Vermaas, and Hans Geerlings. Pathways to industrial-scale fuel out of thin air from CO_2 electrolysis. *Joule*, 3(8):1822–1834, 2019.

[4] Jaya Verma and Saurav Goel. Cost-effective electrocatalysts for hydrogen evolution reactions (HER): challenges and prospects. *International Journal of Hydrogen Energy*, 47(92):38964–38982, 2022.

[5] Daniel P Tabor, Loïc M Roch, Semion K Saikin, Christoph Kreisbeck, Dennis Sheberla, Joseph H Montoya, Shyam Dwaraknath, Muratahan Aykol, Carlos Ortiz, Hermann Tribukait, et al. Accelerating the discovery of materials for clean energy in the era of smart automation. *Nature reviews materials*, 3(5):5–20, 2018.

[6] David Farrusseng. High-throughput heterogeneous catalysis. *Surface Science Reports*, 63(11):487–513, 2008.

[7] Selim Senkan. Combinatorial heterogeneous catalysis—a new path in an old field. *Angewandte Chemie International Edition*, 40(2):312–329, 2001.

[8] Katherine McCullough, Travis Williams, Kathleen Mingle, Pooyan Jamshidi, and Jochen Lauterbach. High-throughput experimentation meets artificial intelligence: a new pathway to catalyst discovery. *Physical Chemistry Chemical Physics*, 22(20):11174–11196, 2020.

[9] Susannah L Scott, T Brent Gunnoe, Paolo Fornasiero, and Cathleen M Crudden. To err is human; to reproduce takes time, 2022.

[10] Abebe Reda Woldu, Zanling Huang, Pengxiang Zhao, Liangsheng Hu, and Didier Astruc. Electrochemical CO_2 reduction (CO_2RR) to multi-carbon products over copper-based catalysts. *Coordination Chemistry Reviews*, 454:214340, 2022.

[11] Jinli Yu, Juan Wang, Yangbo Ma, Jingwen Zhou, Yunhao Wang, Pengyi Lu, Jinwen Yin, Ruquan Ye, Zonglong Zhu, and Zhanxi Fan. Recent progresses in electrochemical carbon dioxide reduction on copper-based catalysts toward multicarbon products. *Advanced Functional Materials*, 31(37):2102151, 2021.

[12] C Lawrence Zitnick, Lowik Chanussot, Abhishek Das, Siddharth Goyal, Javier Heras-Domingo, Caleb Ho, Weihua Hu, Thibaut Lavril, Aini Palizhati, Morgane Riviere, et al. An introduction to electrocatalyst design using machine learning for renewable energy storage. *arXiv preprint arXiv:2010.09435*, 2020.

[13] Janice Lan, Aini Palizhati, Muhammed Shuaibi, Brandon M. Wood, Brook Wander, Abhishek Das, Matt Uyttendaele, C Lawrence Zitnick, and Zachary W. Ulissi. AdsorbML: a leap in efficiency for adsorption energy calculations using generalizable machine learning potentials. *npj Computational Materials*, 9(1):172, 2023.

[14] Brook Wander, Muhammed Shuaibi, John R Kitchin, Zachary W Ulissi, and C Lawrence Zitnick. CatTSunami: Accelerating transition state energy calculations with pre-trained graph neural networks. *arXiv pre-print arxiv:2405.02078*, 2024.

[15] Amil Merchant, Simon Batzner, Samuel S Schoenholz, Muratahan Aykol, Gowoon Cheon, and Ekin Dogus Cubuk. Scaling deep learning for materials discovery. *Nature*, 624(7990):80–85, 2023.

[16] Han Yang, Chenxi Hu, Yichi Zhou, Xixian Liu, Yu Shi, Jielan Li, Guanzhi Li, Zekun Chen, Shuizhou Chen, Claudio Zeni, et al. Mattersim: A deep learning atomistic model across elements, temperatures and pressures. *arXiv preprint arXiv:2405.04967*, 2024.

[17] John Jumper, Richard Evans, Alexander Pritzel, Tim Green, Michael Figurnov, Olaf Ronneberger, Kathryn Tunyasuvunakool, Russ Bates, Augustin Žídek, Anna Potapenko, et al. Highly accurate protein structure prediction with AlphaFold. *Nature*, 596(7873):583–589, 2021.

[18] Zeming Lin, Halil Akin, Roshan Rao, Brian Hie, Zhongkai Zhu, Wenting Lu, Nikita Smetanin, Robert Verkuil, Ori Kabeli, Yaniv Shmueli, et al. Evolutionary-scale prediction of atomic-level protein structure with a language model. *Science*, 379(6637):1123–1130, 2023.

[19] Abhimanyu Dubey, Abhinav Jauhri, Abhinav Pandey, Abhishek Kadian, Ahmad Al-Dahle, Aiesha Letman, Akhil Mathur, Alan Schelten, Amy Yang, Angela Fan, et al. The llama 3 herd of models. *arXiv preprint arXiv:2407.21783*, 2024.

[20] Josh Achiam, Steven Adler, Sandhini Agarwal, Lama Ahmad, Ilge Akkaya, Florencia Leoni Aleman, Diogo Almeida, Janko Altenschmidt, Sam Altman, Shyamal Anadkat, et al. GPT-4 technical report. *arXiv preprint arXiv:2303.08774*, 2023.

[21] Anubhav Jain, Shyue Ping Ong, Geoffroy Hautier, Wei Chen, William Davidson Richards, Stephen Dacek, Shreyas Cholia, Dan Gunter, David Skinner, Gerbrand Ceder, et al. Commentary: The materials project: A materials genome approach to accelerating materials innovation. *APL materials*, 1(1):011002, 2013.

[22] Lowik Chanussot, Abhishek Das, Siddharth Goyal, Thibaut Lavril, Muhammed Shuaibi, Morgane Riviere, Kevin Tran, Javier Heras-Domingo, Caleb Ho, Weihua Hu, et al. Open Catalyst 2020 (OC20) dataset and community challenges. *ACS Catalysis*, 11(10):6059–6072, 2021.

[23] James E Saal, Scott Kirklin, Muratahan Aykol, Bryce Meredig, and Christopher Wolverton. Materials design and discovery with high-throughput density functional theory: the open quantum materials database (OQMD). *JOM*, 65:1501–1509, 2013.

[24] Scott Kirklin, James E Saal, Bryce Meredig, Alex Thompson, Jeff W Doak, Muratahan Aykol, Stephan Rühl, and Chris Wolverton. The open quantum materials database (OQMD): assessing the accuracy of DFT formation energies. *npj Computational Materials*, 1(1):1–15, 2015.

[25] Luis Barroso-Luque, Muhammed Shuaibi, Xiang Fu, Brandon M Wood, Misko Dzamba, Meng Gao, Ammar Rizvi, C Lawrence Zitnick, and Zachary W Ulissi. Open Materials 2024 (OMat24) Inorganic Materials Dataset and Models. *arXiv preprint arXiv:2410.12771*, 2024.

[26] Peter Eastman, Pavan Kumar Behara, David L Dotson, Raimondas Galvelis, John E Herr, Josh T Horton, Yuezhi Mao, John D Chodera, Benjamin P Pritchard, Yuanqing Wang, et al. Spice, a dataset of drug-like molecules and peptides for training machine learning potentials. *Scientific Data*, 10(1):11, 2023.

[27] Justin S Smith, Roman Zubatyuk, Benjamin Nebgen, Nicholas Lubbers, Kipton Barros, Adrian E Roitberg, Olexandr Isayev, and Sergei Tretiak. The ANI-1ccx and ANI-1x data sets, coupled-cluster and density functional theory properties for molecules. *Scientific Data*, 7(1):134, 2020.

[28] Mathias Schreiner, Arghya Bhowmik, Tejs Vegge, Jonas Busk, and Ole Winther. Transition1x-a dataset for building generalizable reactive machine learning potentials. *Scientific Data*, 9(1):779, 2022.

[29] Junrui Li and Shouheng Sun. Intermetallic nanoparticles: Synthetic control and their enhanced electrocatalysis. *Accounts of Chemical Research*, 52(7):2015–2025, 2019. PMID: 31251036.

[30] Joseph H Montoya, Carolyn Grimley, Muratahan Aykol, Colin Ophus, Hadas Sternlicht, Benjamin H Savitzky, Andrew M Minor, Steven B Torrisi, Jackson Goedjen, Ching-Chang Chung, et al. How the AI-assisted discovery and synthesis of a ternary oxide highlights capability gaps in materials science. *Chemical Science*, 15(15):5660–5673, 2024.

[31] Mingjin Cui, Chunpeng Yang, Sooyeon Hwang, Menghao Yang, Sean Overa, Qi Dong, Yonggang Yao, Alexandra H Brozena, David A Cullen, Miaofang Chi, et al. Multi-principal elemental intermetallic nanoparticles synthesized via a disorder-to-order transition. *Science advances*, 8(4):eabm4322, 2022.

[32] Jonathan Schmidt, Noah Hoffmann, Hai-Chen Wang, Pedro Borlido, Pedro JMA Carriço, Tiago FT Cerqueira, Silvana Botti, and Miguel AL Marques. Machine-learning-assisted determination of the global zero-temperature phase diagram of materials. *Advanced Materials*, 35(22):2210788, 2023.

[33] Jonathan Schmidt, Love Pettersson, Claudio Verdozzi, Silvana Botti, and Miguel AL Marques. Crystal graph attention networks for the prediction of stable materials. *Science Advances*, 7(49):eabi7948, 2021.

[34] Johannes Novak Hansen, Hector Prats, Karl Krøjer Toudahl, Niklas Mørch Secher, Karen Chan, Jakob Kibsgaard, and Ib Chorkendorff. Is there anything better than Pt for HER? *ACS Energy Letters*, 6(4):1175–1180, 2021.

[35] Karen Chan. A few basic concepts in electrochemical carbon dioxide reduction. *Nature Communications*, 11(1):5954, 2020.

[36] Yansong Zhou and Boon Siang Yeo. Formation of C–C bonds during electrocatalytic CO_2 reduction on non-copper electrodes. *Journal of Materials Chemistry A*, 8(44):23162–23186, 2020.

[37] Yonggang Yao, Zhennan Huang, Pengfei Xie, Steven D Lacey, Rohit Jiji Jacob, Hua Xie, Fengjuan Chen, Anmin Nie, Tiancheng Pu, Miles Rehwoldt, et al. Carbothermal shock synthesis of high-entropy-alloy nanoparticles. *Science*, 359(6383):1489–1494, 2018.

[38] Talha Kose, Colin P O'Brien, Joshua Wicks, Jehad Abed, Yurou Celine Xiao, Brandon Sutherland, Amitava Sarkar, Shaffiq A Jaffer, Edward H Sargent, and David Sinton. High-throughput parallelized testing of membrane electrode assemblies for CO_2 reduction. *Catalysis Science & Technology*, 12(20):6239–6245, 2022.

[39] Fatemeh Arabyarmohammadi, Rui Kai Miao, Ali Shayesteh Zeraati, Mohammad Zargatalebi, Colin P. O'Brien, Roham Dorakhan, Tartela Alkayyali, Geonhui Lee, Mengyang Fan, Jehad Abed, Feng Li, Edward Sargent, and David Sinton. Voltage distributions within CO_2 electrolyzers. unpublished, 2024. Article under review. Citation will be updated when available.

[40] Jason R Hattrick-Simpers, John M Gregoire, and A Gilad Kusne. Perspective: composition–structure–property mapping in high-throughput experiments: turning data into knowledge. *APL Materials*, 4(5), 2016.

[41] Saulius Gražulis, Adriana Daškevič, Andrius Merkys, Daniel Chateigner, Luca Lutterotti, Miguel Quirós, Nadezhda R. Serebryanaya, Peter Moeck, Robert T. Downs, and Armel Le Bail. Crystallography open

database (cod): an open-access collection of crystal structures and platform for world-wide collaboration. *Nucleic Acids Research*, 40(D1):D420–D427, 2012.

[42] LB McCusker, RB Von Dreele, DE Cox, D Louër, and P Scardi. Rietveld refinement guidelines. *Journal of Applied Crystallography*, 32(1):36–50, 1999.

[43] Pedro Baptista de Castro, Kensei Terashima, Miren Garbine Esparza Echevarria, Hiroyuki Takeya, and Yoshihiko Takano. Xerus: An open-source tool for quick XRD phase identification and refinement automation. *Advanced Theory and Simulations*, 5(5):2100588, 2022.

[44] Keisuke Suzuki, Takashi Toyao, Zen Maeno, Satoru Takakusagi, Ken-ichi Shimizu, and Ichigaku Takigawa. Statistical analysis and discovery of heterogeneous catalysts based on machine learning from diverse published data. *ChemCatChem*, 11(18):4537–4547, 2019.

[45] Shinya Mine, Motoshi Takao, Taichi Yamaguchi, Takashi Toyao, Zen Maeno, SMA Hakim Siddiki, Satoru Takakusagi, Ken-ichi Shimizu, and Ichigaku Takigawa. Analysis of updated literature data up to 2019 on the oxidative coupling of methane using an extrapolative machine-learning method to identify novel catalysts. *ChemCatChem*, 13(16):3636–3655, 2021.

[46] Shinya Mine, Yuan Jing, Takumi Mukaiyama, Motoshi Takao, Zen Maeno, Ken-ichi Shimizu, Ichigaku Takigawa, and Takashi Toyao. Machine learning analysis of literature data on the water gas shift reaction toward extrapolative prediction of novel catalysts. *Chemistry Letters*, 51(3):269–273, 2022.

[47] Travis Williams, Katherine McCullough, and Jochen A Lauterbach. Enabling catalyst discovery through machine learning and high-throughput experimentation. *Chemistry of Materials*, 32(1):157–165, 2019.

[48] Shuo Wang, Lei Li, Jing Li, Chengzong Yuan, Yao Kang, Kwan San Hui, Jintao Zhang, Feng Bin, Xi Fan, Fuming Chen, et al. High-throughput screening of nitrogen-coordinated bimetal catalysts for multielectron reduction of CO_2 to CH_4 with high selectivity and low limiting potential. *The Journal of Physical Chemistry C*, 125(13):7155–7165, 2021.

[49] Manu Suvarna, Tangsheng Zou, Sok Ho Chong, Yuzhen Ge, Antonio J Martín, and Javier Pérez-Ramírez. Active learning streamlines development of high performance catalysts for higher alcohol synthesis. *Nature Communications*, 15(1):5844, 2024.

[50] Ambarish Kulkarni, Samira Siahrostami, Anjli Patel, and Jens K Nørskov. Understanding catalytic activity trends in the oxygen reduction reaction. *Chemical reviews*, 118(5):2302–2312, 2018.

[51] Jens Kehlet Nørskov, Thomas Bligaard, Ashildur Logadottir, JR Kitchin, Jingguang G Chen, S Pandelov, and U Stimming. Trends in the exchange current for hydrogen evolution. *Journal of The Electrochemical Society*, 152(3):J23, 2005.

[52] Allegra A Latimer, Ambarish R Kulkarni, Hassan Aljama, Joseph H Montoya, Jong Suk Yoo, Charlie Tsai, Frank Abild-Pedersen, Felix Studt, and Jens K Nørskov. Understanding trends in C–H bond activation in heterogeneous catalysis. *Nature Materials*, 16(2):225–229, 2017.

[53] Brook Wander, Kirby Broderick, and Zachary W Ulissi. Catlas: an automated framework for catalyst discovery demonstrated for direct syngas conversion. *Catalysis Science & Technology*, 12(20):6256–6267, 2022.

[54] Richard Tran, Duo Wang, Ryan Kingsbury, Aini Palizhati, Kristin Aslaug Persson, Anubhav Jain, and Zachary W Ulissi. Screening of bimetallic electrocatalysts for water purification with machine learning. *The Journal of chemical physics*, 157(7), 2022.

[55] Tong Yang, Jun Zhou, Ting Ting Song, Lei Shen, Yuan Ping Feng, and Ming Yang. High-throughput identification of exfoliable two-dimensional materials with active basal planes for hydrogen evolution. *ACS Energy Letters*, 5(7):2313–2321, 2020.

[56] Mohammad Zafari, Deepak Kumar, Muhammad Umer, and Kwang S. Kim. Machine learning-based high throughput screening for nitrogen fixation on boron-doped single atom catalysts. *J. Mater. Chem. A*, 8:5209–5216, 2020.

[57] Tong Yang, Ting Ting Song, Jun Zhou, Shijie Wang, Dongzhi Chi, Lei Shen, Ming Yang, and Yuan Ping Feng. High-throughput screening of transition metal single atom catalysts anchored on molybdenum disulfide for nitrogen fixation. *Nano Energy*, 68:104304, 2020.

[58] Xingshuai Lv, Wei Wei, Baibiao Huang, Ying Dai, and Thomas Frauenheim. High-throughput screening of synergistic transition metal dual-atom catalysts for efficient nitrogen fixation. *Nano Letters*, 21(4):1871–1878, 2021. PMID: 33587621.

[59] Jeff Greeley, Thomas F Jaramillo, Jacob Bonde, IB Chorkendorff, and Jens K Nørskov. Computational high-throughput screening of electrocatalytic materials for hydrogen evolution. *Nature Materials*, 5(11):909–913, 2006.

[60] Miao Zhong, Kevin Tran, Yimeng Min, Chuanhao Wang, Ziyun Wang, Cao-Thang Dinh, Phil De Luna, Zongqian Yu, Armin Sedighian Rasouli, Peter Brodersen, et al. Accelerated discovery of CO_2 electrocatalysts using active machine learning. *Nature*, 581(7807):178–183, 2020.

[61] Anjli M Patel, Jens K Nørskov, Kristin A Persson, and Joseph H Montoya. Efficient pourbaix diagrams of many-element compounds. *Physical Chemistry Chemical Physics*, 21(45):25323–25327, 2019.

[62] Shyue Ping Ong, William Davidson Richards, Anubhav Jain, Geoffroy Hautier, Michael Kocher, Shreyas Cholia, Dan Gunter, Vincent L Chevrier, Kristin A Persson, and Gerbrand Ceder. Python materials genomics (pymatgen): A robust, open-source python library for materials analysis. *Computational Materials Science*, 68:314–319, 2013.

[63] Arunima K Singh, Lan Zhou, Aniketa Shinde, Santosh K Suram, Joseph H Montoya, Donald Winston, John M Gregoire, and Kristin A Persson. Electrochemical stability of metastable materials. *Chemistry of Materials*, 29(23):10159–10167, 2017.

[64] Alexander Bagger, Wen Ju, Ana Sofia Varela, Peter Strasser, and Jan Rossmeisl. Electrochemical CO_2 reduction: a classification problem. *ChemPhysChem*, 18(22):3266–3273, 2017.

[65] Hongjie Peng, Michael T Tang, Xinyan Liu, Philomena Schlexer Lamoureux, Michal Bajdich, and Frank Abild-Pedersen. The role of atomic carbon in directing electrochemical CO_2 reduction to multicarbon products. *Energy & Environmental Science*, 14(1):473–482, 2021.

[66] Xinyan Liu, Jianping Xiao, Hongjie Peng, Xin Hong, Karen Chan, and Jens K Nørskov. Understanding trends in electrochemical carbon dioxide reduction rates. *Nature Communications*, 8(1):15438, 2017.

[67] Logan Ward, Alexander Dunn, Alireza Faghaninia, Nils ER Zimmermann, Saurabh Bajaj, Qi Wang, Joseph Montoya, Jiming Chen, Kyle Bystrom, Maxwell Dylla, et al. Matminer: An open source toolkit for materials data mining. *Computational Materials Science*, 152:60–69, 2018.

[68] Franklin Tao and Miquel Salmeron. In situ studies of chemistry and structure of materials in reactive environments. *Science*, 331(6014):171–174, 2011.

[69] Spiros Zafeiratos, Simone Piccinin, and Detre Teschner. Alloys in catalysis: phase separation and surface segregation phenomena in response to the reactive environment. *Catalysis Science & Technology*, 2(9):1787–1801, 2012.

[70] E Ringe, Richard P Van Duyne, and LD Marks. Wulff construction for alloy nanoparticles. *Nano letters*, 11(8):3399–3403, 2011.

[71] Roland Lvovich Dobrushin, Roman Kotecký, and Senya Shlosman. *Wulff construction: a global shape from local interaction*, volume 104. American Mathematical Society Providence, 1992.

[72] Richard Tran, Zihan Xu, Balachandran Radhakrishnan, Donald Winston, Wenhao Sun, Kristin A Persson, and Shyue Ping Ong. Surface energies of elemental crystals. *Scientific Data*, 3(1):1–13, 2016.

[73] F. Pedregosa, G. Varoquaux, A. Gramfort, V. Michel, B. Thirion, O. Grisel, M. Blondel, P. Prettenhofer, R. Weiss, V. Dubourg, J. Vanderplas, A. Passos, D. Cournapeau, M. Brucher, M. Perrot, and E. Duchesnay. Scikit-learn: Machine learning in Python. *Journal of Machine Learning Research*, 12:2825–2830, 2011.

[74] Lars Buitinck, Gilles Louppe, Mathieu Blondel, Fabian Pedregosa, Andreas Mueller, Olivier Grisel, Vlad Niculae, Peter Prettenhofer, Alexandre Gramfort, Jaques Grobler, Robert Layton, Jake VanderPlas, Arnaud Joly, Brian Holt, and Gaël Varoquaux. API design for machine learning software: experiences from the scikit-learn project. In *ECML PKDD Workshop: Languages for Data Mining and Machine Learning*, pages 108–122, 2013.

[75] Tianqi Chen and Carlos Guestrin. XGBoost: A scalable tree boosting system. In *Proceedings of the 22nd ACM SIGKDD international conference on knowledge discovery and data mining*, pages 785–794, 2016.

[76] Carlos G Morales-Guio and Xile Hu. Amorphous molybdenum sulfides as hydrogen evolution catalysts. *Accounts of chemical research*, 47(8):2671–2681, 2014.

[77] Ya Yan, BaoYu Xia, Zhichuan Xu, and Xin Wang. Recent development of molybdenum sulfides as advanced electrocatalysts for hydrogen evolution reaction. *ACS Catalysis*, 4(6):1693–1705, 2014.

[78] Jesse D Benck, Thomas R Hellstern, Jakob Kibsgaard, Pongkarn Chakthranont, and Thomas F Jaramillo. Catalyzing the hydrogen evolution reaction (HER) with molybdenum sulfide nanomaterials. *ACS Catalysis*, 4(11):3957–3971, 2014.

[79] Ik Seon Kwon, In Hye Kwak, Tekalign Terfa Debela, Hafiz Ghulam Abbas, Yun Chang Park, Jae-pyoung Ahn, Jeunghee Park, and Hong Seok Kang. Se-rich $MoSe_2$ nanosheets and their superior electrocatalytic performance for hydrogen evolution reaction. *ACS Nano*, 14(5):6295–6304, 2020.

[80] Yoshio Hori, Hidetoshi Wakebe, Toshio Tsukamoto, and Osamu Koga. Electrocatalytic process of CO selectivity in electrochemical reduction of CO_2 at metal electrodes in aqueous media. *Electrochimica Acta*, 39(11-12):1833–1839, 1994.

[81] Kendra P Kuhl, Toru Hatsukade, Etosha R Cave, David N Abram, Jakob Kibsgaard, and Thomas F Jaramillo. Electrocatalytic conversion of carbon dioxide to methane and methanol on transition metal surfaces. *Journal of the American Chemical Society*, 136(40):14107–14113, 2014.

[82] Julia Schumann, Andrew J Medford, Jong Suk Yoo, Zhi-Jian Zhao, Pallavi Bothra, Ang Cao, Felix Studt, Frank Abild-Pedersen, and Jens K Nørskov. Selectivity of synthesis gas conversion to C_{2+} oxygenates on fcc (111) transition-metal surfaces. *ACS Catalysis*, 8(4):3447–3453, 2018.

[83] Aleksandra Vojvodic, Andrew James Medford, Felix Studt, Frank Abild-Pedersen, Tuhin Suvra Khan, T Bligaard, and JK Nørskov. Exploring the limits: A low-pressure, low-temperature Haber–Bosch process. *Chemical Physics Letters*, 598:108–112, 2014.

[84] Joshua T Billy and Anne C Co. Experimental parameters influencing hydrocarbon selectivity during the electrochemical conversion of CO_2. *ACS Catalysis*, 7(12):8467–8479, 2017.

[85] Robert B Sandberg, Joseph H Montoya, Karen Chan, and Jens K Nørskov. CO-CO coupling on Cu facets: Coverage, strain and field effects. *Surface Science*, 654:56–62, 2016.

[86] Leanne D Chen, Makoto Urushihara, Karen Chan, and Jens K Nørskov. Electric field effects in electrochemical CO_2 reduction. *ACS Catalysis*, 6(10):7133–7139, 2016.

[87] Xinyan Liu, Philomena Schlexer, Jianping Xiao, Yongfei Ji, Lei Wang, Robert B Sandberg, Michael Tang, Kristopher S Brown, Hongjie Peng, Stefan Ringe, et al. pH effects on the electrochemical reduction of $CO_{(2)}$ towards C_2 products on stepped copper. *Nature Communications*, 10(1):32, 2019.

[88] Aoni Xu, Nitish Govindarajan, Georg Kastlunger, Sudarshan Vijay, and Karen Chan. Theories for electrolyte effects in CO_2 electroreduction. *Accounts of Chemical Research*, 55(4):495–503, 2022.

[89] Paul J Dyson and Philip G Jessop. Solvent effects in catalysis: rational improvements of catalysts via manipulation of solvent interactions. *Catalysis Science & Technology*, 6(10):3302–3316, 2016.

[90] Mohammad Saleheen and Andreas Heyden. Liquid-phase modeling in heterogeneous catalysis, 2018.

[91] Wanyu Deng, Peng Zhang, Yu Qiao, Georg Kastlunger, Nitish Govindarajan, Aoni Xu, Ib Chorkendorff, Brian Seger, and Jinlong Gong. Unraveling the rate-determining step of C_{2+} products during electrochemical CO reduction. *Nature Communications*, 15(1):892, 2024.

[92] Thao TH Hoang, Sumit Verma, Sichao Ma, Tim T Fister, Janis Timoshenko, Anatoly I Frenkel, Paul JA Kenis, and Andrew A Gewirth. Nanoporous copper–silver alloys by additive-controlled electrodeposition for the selective electroreduction of CO_2 to ethylene and ethanol. *Journal of the American Chemical Society*, 140(17):5791–5797, 2018.

[93] Ye Eun Jeon, You Na Ko, Jongseok Kim, Hyuk Choi, Wonhee Lee, Young Eun Kim, Doohwan Lee, Hyun You Kim, and Ki Tae Park. Selective production of ethylene from CO_2 over CuAg tandem electrocatalysts. *Journal of Industrial and Engineering Chemistry*, 116:191–198, 2022.

[94] Dan Ren, Bridget Su-Hui Ang, and Boon Siang Yeo. Tuning the selectivity of carbon dioxide electroreduction toward ethanol on oxide-derived Cu_xZn catalysts. *ACS Catalysis*, 6(12):8239–8247, 2016.

[95] Weiwei Zhu, Kuangmin Zhao, Suqin Liu, Min Liu, Feng Peng, Pengda An, Binhao Qin, Huimin Zhou, Hongmei Li, and Zhen He. Low-overpotential selective reduction of CO_2 to ethanol on electrodeposited Cu_xAu_y nanowire arrays. *Journal of Energy Chemistry*, 37:176–182, 2019.

[96] Sichao Ma, Masaaki Sadakiyo, Minako Heima, Raymond Luo, Richard T Haasch, Jake I Gold, Miho Yamauchi, and Paul JA Kenis. Electroreduction of carbon dioxide to hydrocarbons using bimetallic Cu-Pd catalysts with different mixing patterns. *Journal of the American Chemical Society*, 139(1):47–50, 2017.

[97] Apurv Saxena, Wipula Liyanage, Jahangir Masud, Shubhender Kapila, and Manashi Nath. Selective electroreduction of CO_2 to carbon-rich products with a simple binary copper selenide electrocatalyst. *Journal of Materials Chemistry A*, 9(11):7150–7161, 2021.

[98] Apurv Saxena, Wipula PR Liyanage, Shubhender Kapila, and Manashi Nath. Nickel selenide as an efficient electrocatalyst for selective reduction of carbon dioxide to carbon-rich products. *Catalysis Science & Technology*, 12(15):4727–4739, 2022.

[99] Apurv Saxena, Shubhender Kapila, Julia E Medvedeva, and Manashi Nath. Copper cobalt selenide as a bifunctional electrocatalyst for the selective reduction of CO_2 to carbon-rich products and alcohol oxidation. *ACS Applied Materials & Interfaces*, 15(11):14433–14446, 2023.

[100] Dexin Yang, Qinggong Zhu, Chunjun Chen, Huizhen Liu, Zhimin Liu, Zhijuan Zhao, Xiaoyu Zhang, Shoujie Liu, and Buxing Han. Selective electroreduction of carbon dioxide to methanol on copper selenide nanocatalysts. *Nature Communications*, 10(1):677, 2019.

[101] Apurv Saxena, Harish Singh, and Manashi Nath. Cobalt telluride electrocatalyst for selective electroreduction of CO_2 to value-added chemicals. *Materials for Renewable and Sustainable Energy*, 11(2):115–129, 2022.

[102] Jingfu He, Noah JJ Johnson, Aoxue Huang, and Curtis P Berlinguette. Electrocatalytic alloys for CO_2 reduction. *ChemSusChem*, 11(1):48–57, 2018.

[103] Daniel A Torelli, Sonja A Francis, J Chance Crompton, Alnald Javier, Jonathan R Thompson, Bruce S Brunschwig, Manuel P Soriaga, and Nathan S Lewis. Nickel–gallium-catalyzed electrochemical reduction of CO_2 to highly reduced products at low overpotentials. *ACS Catalysis*, 6(3):2100–2104, 2016.

[104] Daniël van den Berg, Johannes C Brouwer, Ruud WA Hendrikx, and Ruud Kortlever. Experimental screening of intermetallic alloys for electrochemical CO_2 reduction. *Catalysis Today*, 439:114805, 2024.

[105] Arnaud Thevenon, Alonso Rosas-Hernández, Alex M Fontani Herreros, Theodor Agapie, and Jonas C Peters. Dramatic HER suppression on Ag electrodes via molecular films for highly selective CO_2 to CO reduction. *ACS Catalysis*, 11(8):4530–4537, 2021.

[106] Haiwen Dai, Sofia Dimitriadou, PS Sankara Rama Krishnan, Albertus Denny Handoko, Jose Recatala-Gomez, Yong Wang, DV Maheswar Repaka, Maung Thway, Chenguang Zhang, Martial Duchamp, et al.

Sub-10 nm mixing and alloying of cu–ag and cu–ni via accelerated solid diffusion. *ACS Applied Materials & Interfaces*, 15(23):28398–28409, 2023.

[107] Fen Zhang and Anne C Co. Direct evidence of local pH change and the role of alkali cation during CO_2 electroreduction in aqueous media. *Angewandte Chemie International Edition*, 59(4):1674–1681, 2020.

[108] Jacob R Boes, Osman Mamun, Kirsten Winther, and Thomas Bligaard. Graph theory approach to high-throughput surface adsorption structure generation. *The Journal of Physical Chemistry A*, 123(11):2281–2285, 2019.

[109] Johannes Gasteiger, Muhammed Shuaibi, Anuroop Sriram, Stephan Günnemann, Zachary Ulissi, C Lawrence Zitnick, and Abhishek Das. GemNet-OC: developing graph neural networks for large and diverse molecular simulation datasets. *arXiv preprint arXiv:2204.02782*, 2022.

[110] Georg Kresse and Jürgen Hafner. Ab initio molecular-dynamics simulation of the liquid-metal–amorphous-semiconductor transition in germanium. *Physical Review B*, 49(20):14251–14269, 1994.

[111] Georg Kresse and Jürgen Furthmüller. Efficient iterative schemes for ab initio total-energy calculations using a plane-wave basis set. *Physical Review B*, 54(16):11169–11186, 1996.

[112] "The calculations in this work have been performed using the ab-initio total-energy and molecular- dynamics package VASP (Vienna ab-initio simulation package) developed at the Institut für Materialphysik of the Universiät Wien2,3.".

[113] Georg Kresse and Daniel Joubert. From ultrasoft pseudopotentials to the projector augmented-wave method. *Physical Review B*, 59(3):1758, 1999.

[114] Georg Kresse and Jürgen Furthmüller. Efficiency of ab-initio total energy calculations for metals and semiconductors using a plane-wave basis set. *Computational Materials Science*, 6(1):15–50, 1996.

Appendix

A Experimental Studies

A.1 Experimental Material Selection

Diversity is essential when creating training data for ML models. In our experimental studies, this includes the diversity of the elemental composition and the diversity of the products produced when they are used as catalysts. To increase the likelihood of sampling materials that produce different products, we grouped the materials into three rough groups and attempted to sample them equally. For CO_2RR, we devised a multi-objective optimization framework to suggest materials that are likely to produce multi-carbon products. Through this analysis, we selected 317 compositions as possible C_{2+} candidates based on the following scoring function:

$$score = w_1||E_{CO} + 0.67||_2 + w_2||E_H - 0.15||_2 + w_3(E_{COCOH} - 2E_{CO}) \quad (6)$$

Here, E_x corresponds to the computationally calculated adsorption energy of a particular adsorbate. The three terms in Equation (6) correspond to (1) targeting a CO adsorption energy near -0.67 eV, (2) targeting a H adsorption energy near 0.15 eV, and (3) favoring COCOH binding affinity over CO. Each term is normalized to ensure that similar distributions do not bias the overall objective function and objective weights w_i are used to place more importance on descriptors. Initially, these weights are set to $w_i = 1$, but could have been updated in response to experimental findings. Once all surfaces have been assigned a score, we classify the top 10% of the materials as C_{2+} candidates.

Missing from the expected outcome is the presence of many C_{2+} classified Cu alloys. There are only five such alloys out of the 317 selected. This could be a reflection of some failing in the framework, but it was intentionally not optimized with this in mind. There is literature precedent for certain Cu alloys experimentally showing a propensity towards multi-carbon products, but often those materials are not ordered intermetallics [92–96] like those considered here. There are also a modest number of materials containing chalcogens that have been classified as possible C_{2+} producers. There is literature precedent for Se and Te alloys producing multi-carbon products [97–99], but they have also been shown to produce other C_1 products [100,101]. The product selectivity for this family of materials appears to be very sensitive to exact composition ratios and reaction conditions. The prospect of discovering multicarbon selective alloys composed of earth-abundant elements such as Ga and Zn is exciting, but alloys studied containing these elements have been shown to suffer from poor Faradaic efficiencies [102]. Nickel gallium alloys have been shown to produce multi-carbon products [103] with very low onset potentials, but they suffer from poor selectivity [104]. Without extensive experimental testing, it is unclear whether the materials suggested by the multi-objective framework to be possible C_{2+} producers will be realized as such.

For HER we categorized all compositions with more than 50% of surfaces having H adsorption energies less than -0.1 eV as likely hydrogen producers during CO_2RR. All other compositions were classified as possible C_1 producers. This resulted in 11,916 HER compositions and 3,201 C_1 compositions. Note, these sets of compositions only provide potential candidates for synthesis of which only a subset were selected. At a high level, chemical intuition is retained. For HER, there are a large number of Pt and Pd alloys. This is sensible because unary Pt and Pd are known hydrogen producers [80,81]. For C_1, there are a large number of gold and silver alloys, which as unaries are known to produce carbon monoxide [80,81,105]. For C_1 there is a general shift toward less reactive elements compared to elements that appear frequently for HER. This shift continues for C_{2+} products, which tend more toward post-transition metals and metalloids.

Our goal was to roughly select an equal number of materials from each category (C_{2+}, C_1, and HER). However, the C_{2+} samples proved difficult to synthesize. The accessibility of elements for both synthesis techniques is shown at the top of the Experimental Chemical Space section of Figure 3. For spark ablation, there were substantial oxidation issues when synthesizing Zn, In, and Sn. Gallium was also difficult to incorporate because it has a low melting temperature. These four elements were present in nearly all of the materials that we classified as possible multi-carbon producers. For chemical reduction, there were similar challenges

preparing samples that were classified as possible multi-carbon and C_1. Note, while Pt was accessible to our synthesis techniques, no samples were synthesized using Pt in this study.

Our synthesis techniques are limited in their ability to match target compositions with errors up to $10\% - 15\%$. Due to this, additional samples were synthesized in the "gaps" between target compositions. This increased the likelihood that samples would be synthesized close to the target compositions, as verified by XRF. A byproduct of this approach is that a considerable number of synthesized samples are not in the three categories above (C_1, C_{2+}, and HER).

A.2 Spark Ablation Synthesis

A.2.1 Printing of nanoporous films

In this work, the VSP-P1 Nanoprinter was used to synthesize inorganic nanoporous thin films with different binary and ternary elemental composition. The P1 uses three sequential automated steps to convert a solid rod into particles smaller than 5 nm and print them in the form of nanoporous layers.

In the first step, two solid rods are placed with the tips closely spaced to each other. Electrical sparks are formed between the rods to create a local plasma. Due to the high temperature of the plasma (>20,000°C), small parts of the rods are evaporated into an atomic cluster. Directly after the spark, the loose atoms bump into each other and grow into bigger clusters/nanoparticles.

In the second step, the evaporated material is transported by a carrier gas that flows in between the electrodes. Since the carrier gas is at room temperature, it accelerates the cooling of the hot gas after the plasma stage. Due to this fast quenching, the particles of the cluster stabilize (e.g. stop aggregating) at 2 – 5 nanometers in size. During their time-of-flight, these stable primary nanoparticles could still form agglomerates by sticking to and colliding with each other.

In the final step, the impaction method is used to get the growing particles out of the carrier gas and printed on a substrate. This is achieved by accelerating the gas flow to supersonic speeds by forcing them through a nozzle with a narrow orifice. At this speed, the growing nanoparticles are not able to follow the gas flow but instead follow a straight trajectory and immobilize on the substrate. In this way, thin-film nanoporous layers of nanoparticles can be formed with different thicknesses. Since the substrate is mounted on an XYZ-gantry stage, the nanoparticles can be printed in all kind of complex patterns. It is important to mention that because of the small size of the nanoparticles, they have a very strong Van der Waals force which make them stick to any surface or other nanoparticles. This unique feature enables the VSP-P1 to print sticking layers on almost any substrate without adding binders.

A dedicated P1 was used for this project with the following specs:

- 3 units of VSP-G1 nanoparticle sources
- Carrier gas: Ar/H2 (95/5)
- Nozzle diameter: 0.55mm
- Flow rate in G1: 1.35 L/m
- Substrate to nozzle distance: 2.4 mm
- Current : 0.1 – 10 mA
- Voltage: 0.5 – 1.3 kV
- Vacuum chamber pressure: 1.65 - 1.70 mbar

(Note: Voltage and current are adjusted according to the desired output to achieve specific loading and alloying ratios)

A.2.2 Calibrating the printer for different materials

Due to differences in evaporation enthalpy, it is important to calibrate the amount of material that is deposited on the substrate. This calibration is specific for element type, electrode diameter, carrier gas type, flow, nozzle

size, and distance between nozzle and substrate. Calibration is performed by printing on carbon paper gas diffusion layer (GDL) (type H23C3 from fuelcellstore.com) for different periods of time and measuring the mass increase. Plotting these points on a graph with an intercept of zero gives a slope that represents the printing rate in milligrams per hour. The calibration is done with two of the VSP-G1 sources connected, including multiple times with cleaning of the G1 in between prints. Calibration was performed under fixed operating conditions: the gas flow rate in both G1s were 1.35 L/min Ar/H2 (95/5), and the spark settings were 1.3 kV and 10 mA with a spark frequency of 220 Hz.

A.2.3 Controlling oxidation of the samples during shipment for electrochemical testing

Since most of the elemental analysis was conducted at the University of Toronto's facilities, we investigated the impact of shipping on the samples. The nanoporous metallic samples were expected to oxidize when exposed to air (oxygen). However, we discovered that packaging the samples under inert gases like Argon still resulted in oxidation, despite using cycles of vacuuming and purging with inert gas. Surprisingly, packaging the samples in air did not lead to oxidation. XRD analysis revealed that the samples remained metallic for more than six days when exposed to air. Annealing the samples under a gas mixture of 95% Ar and 5% H_2 at 400°C for 30 minutes after shipment was found to reduce surface oxides and alloy the metal mixtures [106]. During the annealing process, the particle size is increased gradually until a layer is formed. By optimizing the annealing temperature the alloy can be formed without losing to much of the porosity. Annealing was limited to relatively low temperatures and for short times to prevent nanoparticle growth and reactivity reduction.

A.2.4 Controlling the elemental composition by mixing 2 or 3 sources

A standard VSP-P1 is able to work with 2 VSP-G1 nanoparticle sources. The output of the 2 sources is combined into a single gas stream that is entering the printer nozzle. If one sources is setup with gold electrodes and the other with copper electrodes the P1 is printing nanoporous layers made of stacked gold and copper nanoparticles. For this study, VSP modified the P1 to accommodate a 3rd VSP-G1 source to make ternary compositions as well as binary. The composition of the particles in the gas stream can be tuned by lowering the power settings for one, or two in the case where three sources are used, of the G1s. One G1 is kept at 1.3 kV and 10 mA as max settings. Lowering the output is done by lowering the current and keep the voltage constant. In this way the gap between the electrodes stays constant and only lowers the frequency of sparking. The frequency cannot be set in the G1, but rather it is a result of the combination between voltage and current that is chosen. There is a limit to this, however, if the frequency drops below around 20 Hz the sparking becomes unstable. This happens when the current is below 1.1 mA and the voltage has been lowered to 0.5 kV. The loading/layer thickness is tuned by the movement speed of the stage during printing.

A.2.5 Printing the same elemental composition on wafer and GDE substrates

The initial goal of the synthesis was to deposit sample on a silicon wafer to enable characterization by XRF and XRD without peak interference in the region of interest. This involved printing 2x2 mm squares of various compositions on the wafer, achieving a loading of 0.2 mg/cm^2 by stacking five layers sequentially. Each batch included 25 unique compositions. After annealing the Si wafer, XRD was used to identify the crystal structure of the samples, which were then replicated on gas diffusion electrode (GDE) for performance testing. However, XRF revealed source output deviations of 1-15% from the setpoint, complicating the replication of exact compositions on GDEs. To resolve this, we began printing wafer and GDE samples simultaneously. Each batch included a 4-inch wafer and a 10x10 cm GDE substrate, allowing consistent and stable G1 settings. Layers were alternated between the wafer and GDE to average out compositional drift.

A.3 Chemical Reduction Synthesis

A.3.1 Automated catalyst preparation: wet-chemistry synthesis

The automated synthesis was performed using the Chemspeed Swing XL platform (Figures 8 and 9). Metal precursor stock solutions (0.15 M) and a hydrazine/NaOH(2.67 M) reducing solution (25:27, v/v) were manually prepared and loaded into the platform. Precise ratios of these stock solutions were mixed to achieve the desired compositions (1.5 mL total per tube). After thorough mixing, 0.65 mL of hydrazine/NaOH

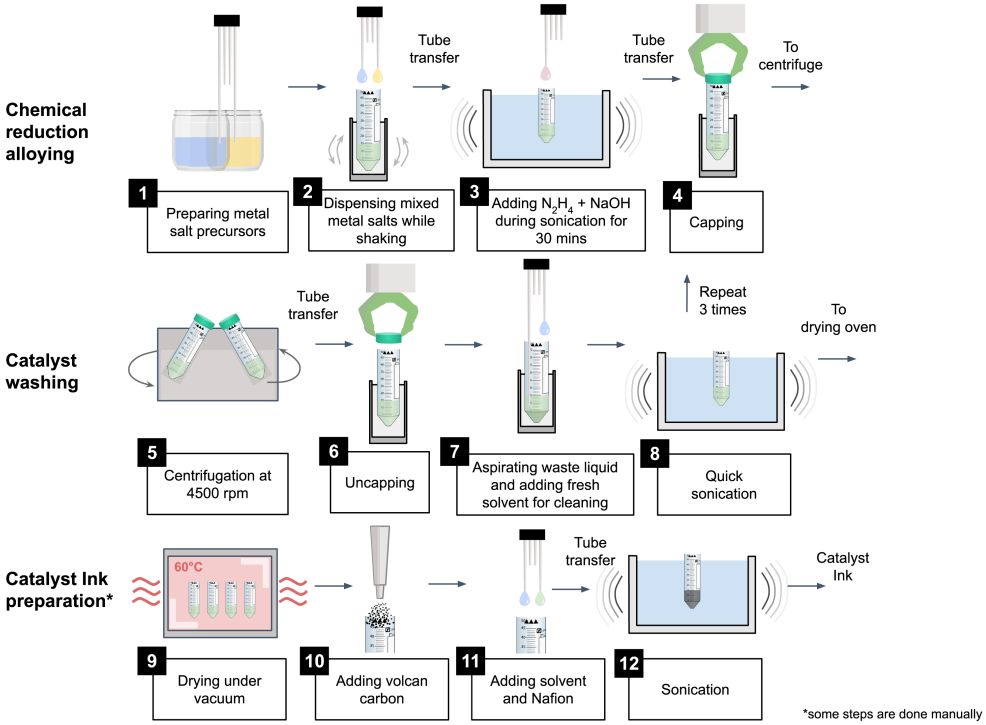

Figure 7 This workflow diagram illustrates the step-by-step process of the chemical reduction synthesis method using the Chemspeed robot.

solution were added and ultrasonicated at 50°C for one hour. The process concluded with three purification cycles involving ultrasonication and deionized (DI) water rinses and, lastly, the solutions were dried in a vacuum oven (Figure 7).

A.3.2 Catalyst annealing

The catalysts prepared via both synthesis approaches were annealed under a mixed gas atmosphere of 5% H2 and 95% Ar (forming gas) to induce the formation of alloys. For spark ablation, samples were annealed after being printed on a Si wafer and GDL. For samples prepared via chemical reduction, the resultant powder was annealed prior to drop-casting on a GDL. Initially, the tube furnace was purged with the forming gas for 3 hours and then the temperature was ramped to 400°C at a rate of 5°C/min, followed by aging at 400°C for 30 minutes. After the heat treatment, the furnace was cooled down to room temperature while continuously purging with forming gas to prevent oxidation of the samples before they were removed from the furnace.

A.3.3 Catalyst ink and electrode Preparation

For the catalysts obtained via chemical reduction synthesis, a catalyst ink was prepared by mixing the synthesized powde with Vulcan carbon XC-72R, Nafion perfluorinated resin solution (5 wt%), and 2-propanol in a ratio of 6 mg : 4 mg : 20 uL : 500 uL. The mixture was then ultrasonicated for 1 hour and drop-casted onto a 1 cm^2 GDL (Freudenberg H23C3).

A.4 Electrochemical Testing

As an improvement to the previously reported testing apparatus[38], gas vials are directly connected to the MEA cells, enabling simultaneous sample collection and streamlining the process. This allows for asynchronous testing by storing samples between runs, ensuring continuous operation without manual transfers to a gas chromatograph (GC). The vials can be unplugged and moved to an autosampler for sequential injection into the GC, enhancing testing throughput and supporting full parallel operation and asynchronous operation.

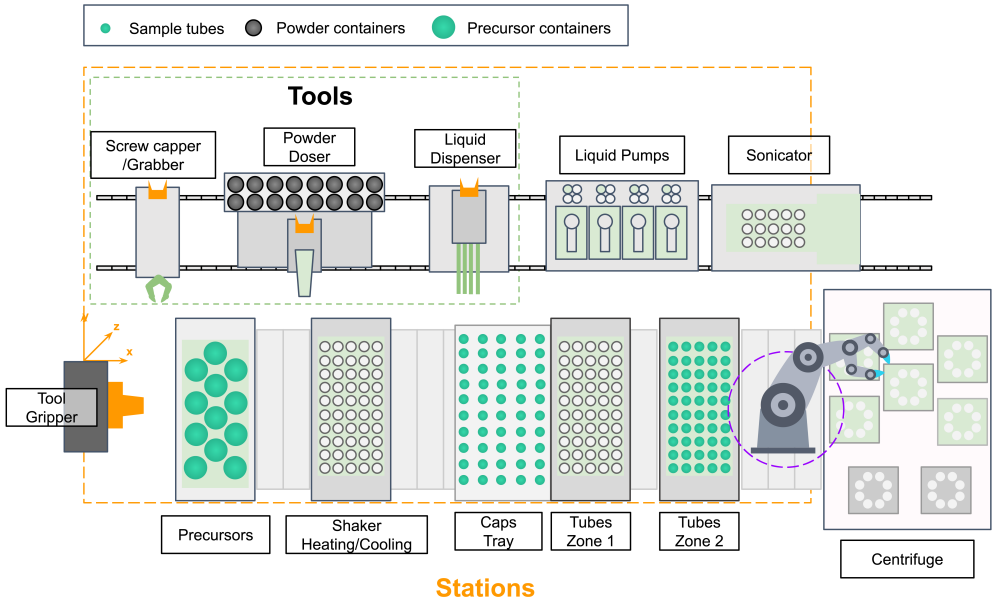

Figure 8 This is a top layout of the Chemspeed robot used for the chemical reduction synthesis.

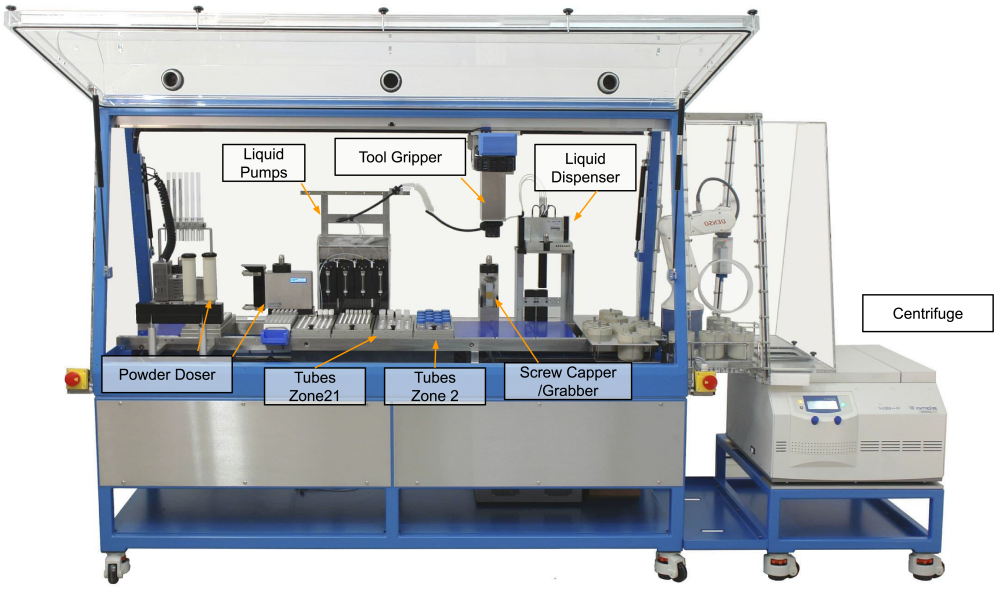

Figure 9 This is a photo of the Chemspeed robot used for the chemical reduction synthesis.

B Characterization

B.1 XRF and XRD experimental setup

X-ray fluorescence spectroscopy (XRF) was conducted using a Fischerscope X-ray XDAL with a microfocus tungsten (W) X-ray tube operating at 50 kV. Each sample was measured three times with an acquisition time of 20 seconds per measurement, while scanning the stage in xy directions. X-ray diffraction (XRD) measurements were performed using a Bruker D8 Discover diffractometer equipped with a Cu microfocus X-ray source ($\lambda = 0.15418$ nm), operating at 50 kV and 1000 μA. A 0.4 mm slit was employed, and data were collected over a 2θ range of 5° to 80° with a step size of 0.04° and a dwell time of 1.2 seconds per increment. The diffraction patterns were recorded at ambient temperature in 1D mode, with the detector aperture set to 62 mm x 20 mm. The Si wafer with multiple catalyst samples was positioned on the measuring stage and the coordinates of five initial samples were determined using the overhead camera built into the diffractometer. A script was used to apply a translation and 2D rotation to calculate the coordinates of the remaining samples.

B.2 XRD analysis

The process begins by cleaning the XRD data to remove background noise and extract clear diffraction patterns. We then fetch computational structures that contain the elements of interest and simulate their XRD patterns using a tool in pymatgen[62]. We use Earth-Mover's distance to calculate how similar these patterns are to the experimental data 10. After identifying a phase, we remove overlapping peaks and repeat the first step until all phases are matched or a set limit is reached 11. Rietveld fitting helps us assess the quality of the match by calculating the weighted profile R score (R_{wp}), which evaluates the quality of the fit 12. This entire process is repeated for a user-defined number of trials to run through a set number of possible phase combinations without excessive computational cost.

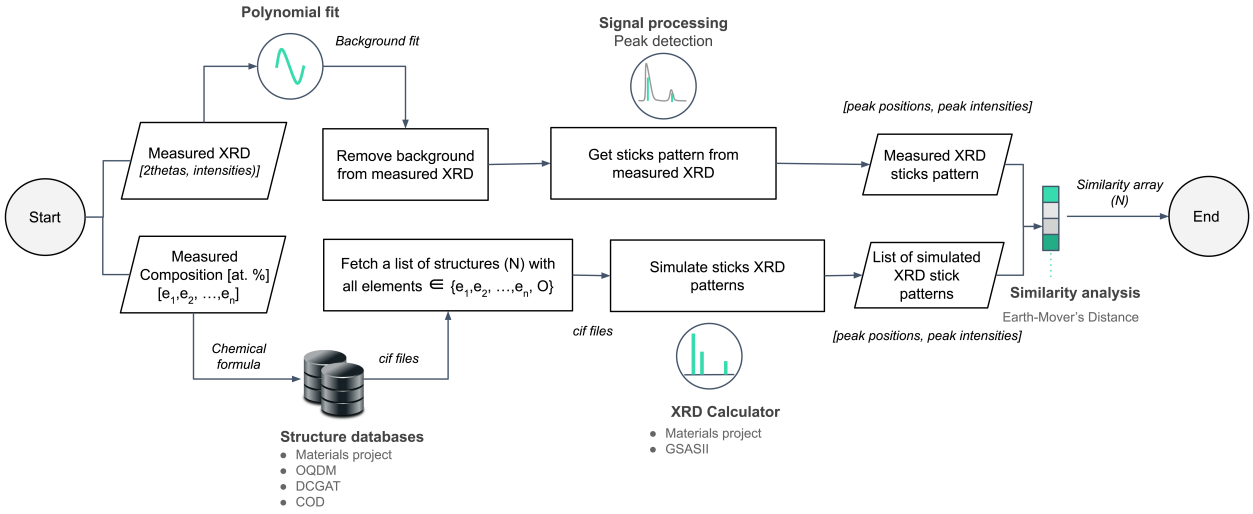

Figure 10 A flowchart of the first step of the XRD analysis pipeline. This steps constructs a similarity analysis using the experimental XRD pattern and a list of simulated XRD patterns from structures that are fetched from Materials Project, OQMD, and Alexandria

C Computational Studies

C.1 Material Selection

We considered all materials available in three permissively-licensed computational materials databases: MP[21], OQMD[23,24], and Alexandria[32,33]. In an effort to improve the likelihood of discovering an industrially viable catalyst, materials were filtered by assessing their thermodynamic stability under reaction conditions. To do

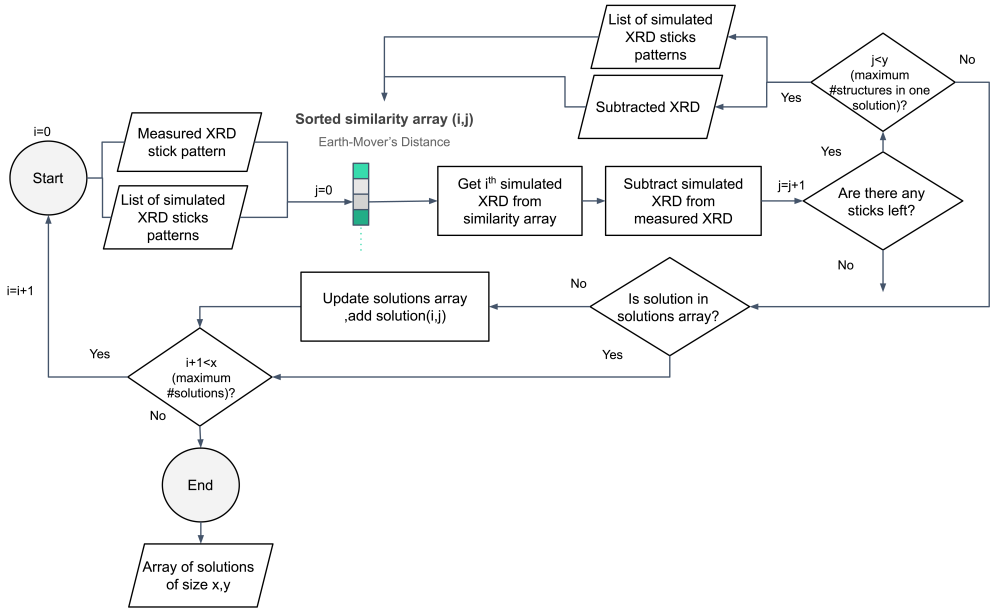

Figure 11 A flowchart showing the iterative process of matching the experimental XRD pattern with multiphases. The process involves iteratively removing matched patterns, updating the experimental pattern, and identifying new matches to add new matched phases.

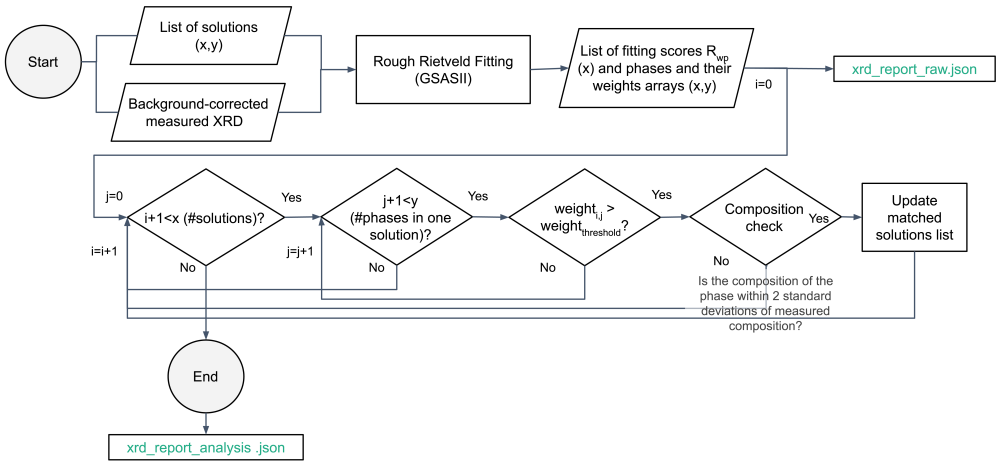

Figure 12 A flowchart showing the final step in the XRD analysis running a Rough Rietveld Refinement to evaluate the goodness of the fit and aid with ranking solutions.

this, we evaluated the decomposition energy using the Pourbaix framework implemented in pymatgen [61–63]. We were interested in neutral pH conditions (in the bulk), but the pH will be elevated at the electrode under operating conditions [84,107]. Materials with a decomposition energy less than 0.05 eV/atom anywhere in the operating range of pH (7 to 14) and applied potential (-1.35 to -0.55 V versus SHE) were retained. To facilitate this analysis despite any small differences in DFT settings, we determined a subset of materials within the non-MP databases with analogous entries in MP. Using the formation energies of these materials in each of the databases, we fit linear corrections to the formation energies to be MP-like (see Figure 16). From the Pourbaix analysis, we found 2,458 materials from MP, 3,173 materials from OQMD, and 13,775 materials from Alexandria for use in our computational pipeline. The bulk materials were then re-optimized with revised Perdew-Burke-Ernzerhof (RPBE) to be consistent with the level of theory of Open Catalyst 2020 Dataset (OC20), which the Machine learning (ML) models used in this work were trained on. We removed materials from Alexandria that have magnetic moments because of an error in calculation. For MP, OQMD, and the

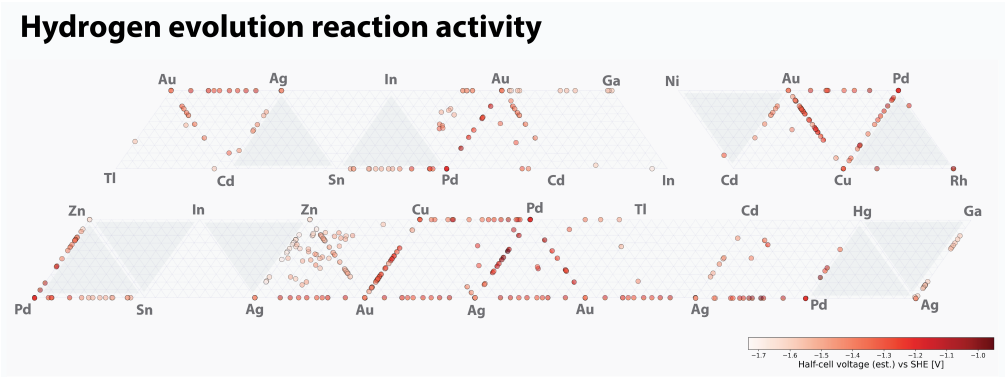

Figure 13 Mapping of half-cell cathodic potential vs SHE for hydrogen evolution reaction Darker shaded ternary phase diagrams result from connecting several diagrams and were not intentionally explored

data used to train the models used for structure optimizations magnetic moments were neglected. For the materials with Alexandria, the bulk optimizations were performed with magnetic moments, an inconsistency with the rest of the pipeline. Still, for better results on magnetic materials they should be handled more appropriately.

C.2 Adsorption Energy Calculations

C.2.1 Adsorbate placements

Catalyst slabs were created from relaxed bulks using pymatgen[62] implemented code to enumerate all surfaces up to Miller index 2. All surface terminations were used for materials from MP and OQMD. For materials from Alexandria, two surface terminations per Miller index were selected: a random termination and the lowest surface energy termination. All surface and placement enumeration code is provided at https://github.com/Open-Catalyst-Project/Open-Catalyst-Dataset. Materials coming from MP and OQMD materials were done from an earlier snapshot of the codebase (commit 17e350e). Alexandria enumeration was performed after a refactor (commit b12aac4), which provided improved random placements and minor fixes throughout. A total of $\sim 700,000$ unique surfaces were generated across the selected materials.

Placements were made with several modes: full heuristic placements, random sites with heuristic placements, and full random placements. For random sites, a Delaunay meshgrid is constructed with sites uniformly sampled across the grid. For heuristic, sites are assigned at each surface atom (atop), between every pair of adjacent surface atoms (bridge), and at the center of every group of three or four adjacent surface atoms (hollow). For all approaches, the adsorbate binding atom is placed onto the site, then the adsorbate is translated along the surface normal until the minimum distance between any adsorbate atom and any surface atom is 0.1 Å. Additionally, to increase the diversity of initial configurations considered, the adsorbate is uniformly randomly rotated around the z-direction and provided a slight wobble around x and y, which amounts to a randomized tilt within a certain cone around the north pole. For even greater diversity, random rotations in all directions about the center of mass are applied for the fully random placement mode. Placements made before updates followed a similar strategy but used CatKit[108] for heuristic placements and restricted random rotations to only the z-axis. These changes were shown to have negligible effect on the performance of adsorption energy calculations, as shown by Lan et al.[13].

C.2.2 ML relaxations

Screening the proposed search space for CO_2RR with DFT would be an intractable problem for even the world's most powerful supercomputers. To address this, recent work[13,22] has demonstrated the utility of generalized ML potentials for catalyst discovery. The incredible progress the community has made in the development of more accurate models has made the reality of large screening campaigns like this possible.

For all adsorbate and surface combinations, we calculate the adsorption energies using an AdsorbML[13] ML+SP

approach. Given an adsorbate-surface combination, we first enumerate ∼165 different adsorbate configurations (100 random + ∼65 heuristic) on the surface. ML relaxations are then performed using GemNet-OC[109], a cost-effective Graph Neural Network (GNN) trained on the OC20 dataset. Unlike a DFT relaxation that can take roughly 24 hours per relaxation, ML models used in this work finish in as little as five seconds. Once the ML relaxed states are computed, the five lowest-energy systems are selected and a single point DFT call is made on the ML relaxed structure to get a more accurate adsorption energy. For an in-depth discussion of the algorithm and model, we refer the readers to the original AdsorbML[13] and GemNet-OC[109] manuscripts. All ML relaxations were run for 200 optimization steps or until a maximum force norm of 0.02 eV/Å is achieved, whichever comes first.

C.2.3 DFT calculations

DFT relaxations were performed consistent with OC20 and AdsorbML. *Vienna Ab initio Simulation Package* (VASP) with projector augmented wave (PAW) pseudopotentials and the RPBE functional were used for all calculations[110–114]. All single-point calculations were performed with a maximum number of electronic steps of 300 to ensure that the initialized wavefunction had sufficient steps to converge. Single-point calculations with unconverged electronic steps were discarded.

C.3 Interpolation to fixed applied potential

All experiments were performed at fixed potentials of 50, 100, 150, 200, and 300 mA/cm^2. To make comparisons with a fixed driving force, a linear interpolation to a fixed potential was applied. A fixed potential of 3.3 V was used, the average potential across all testing experiments. This interpolation was limited so extrapolation would not be performed and was performed in log space, so the relation between voltage and current density should be linear. If the chosen potential occurred at a current density outside of the tested range (50-300 mA/cm^2), then the value at the closest end of the range was taken. This was performed for each sample and the interpolated results were used as targets for the regression models.

C.4 Additional results

The full set of results for both CO_2RR and HER across both cross-validation strategies are summarized in Table 2. Results on CH_4 and C_2H_4 can appear positive but are primarily a result of little to no production, allowing the models to predict near 0 successfully. A larger dataset could remedy this by providing more samples for these products.

C.4.1 HER results

HER results evaluated against LOO and LOCO for a linear model using mean adsorption energy features are presented in Figure 17.

C.4.2 Ethylene results

CO_2RR results evaluated on C_2H_4 are provided in Figure 18. The limited availability of C_{2+} producing samples makes the fitting not particularly meaningful. Similar results are also observed with CH_4.

C.4.3 Linear model

The main paper presented CO_2RR results trained on a random forest model. We also present results using a linear model in Figure 19. The results are considerably worse than random forest.

C.4.4 Matminer-only features

The main paper presented CO_2RR results trained using both Boltzmann-weighted adsorption energies and elemental Matminer features. Figure 20 shows the performance using only Matminer features. The results using only elemental features are very comparable to those also considering adsorption energies.

			LOO		LOCO	
Source	Reaction	Product	R^2	MAE	R^2	MAE
Spark + Reduction	HER	Voltage [V vs SHE]	0.61	0.08	0.59	0.08
	CO2RR	$H_{2,Pr}$ [nmol/cm^{2}s]	0.46	87.82	0.22	112.67
		CO_{Pr}	0.44	67.91	0.01	95.95
		$Liquid_{Pr}$	0.43	55.84	0.18	74.11
		$C_2H_{4,Pr}$	0.08	3.53	0.01	3.83
		$H_{2,FE}$ [%]	0.48	11.99	0.17	16.22
		CO_{FE}	0.55	10.26	0.10	14.96
		$Liquid_{FE}$	0.41	7.30	0.22	9.06
		$C_2H_{4,FE}$	0.43	0.36	0.29	0.43
Spark Ablation	HER	Voltage [V vs SHE]	0.50	0.08	0.34	0.09
	CO2RR	$H_{2,Pr}$ [nmol/cm^{2}s]	0.45	96.86	0.26	124.30
		CO_{Pr}	0.53	60.99	0.01	94.53
		$Liquid_{Pr}$	0.45	51.58	0.03	77.44
		$C_2H_{4,Pr}$	0.00	3.52	0.00	3.60
		$H_{2,FE}$ [%]	0.44	11.31	0.11	15.77
		CO_{FE}	0.57	9.81	0.17	13.99
		$Liquid_{FE}$	0.49	5.32	0.08	7.82
		$C_2H_{4,FE}$	0.01	0.48	0.00	0.55
Chemical Reduction	HER	Voltage [V vs SHE]	0.66	0.07	0.65	0.07
	CO2RR	$H_{2,Pr}$ [nmol/cm^{2}s]	0.30	70.99	0.12	86.69
		CO_{Pr}	0.40	69.71	0.00	103.27
		$Liquid_{Pr}$	0.33	67.00	0.27	73.87
		$C_2H_{4,Pr}$	0.42	3.58	0.15	4.02
		$H_{2,FE}$ [%]	0.40	14.63	0.07	19.88
		CO_{FE}	0.48	11.17	0.02	16.34
		$Liquid_{FE}$	0.48	8.09	0.41	9.37
		$C_2H_{4,FE}$	0.89	0.20	0.81	0.27

Table 2 Full predictive results for CO_2RR and HER across the different synthesis techniques. A linear model using only mean adsorption energy features was used for HER and a random forest model using Boltzmann weighted adsorption energy and Matminer features for CO_2RR, representing the best results explored in this work. CH_4 results were excluded because very little product was produced to make reliable predictive assessments.

C.4.5 Matched-only features

The main paper presented CO_2RR results fitted on both XRD matched and unmatched data. The results of fitting a model on only the XRD matched data are shown in Figure 21. Fitting on both matched and unmatched data tends to help our predictive models and they are more performant than only fitting on XRD matched data. This is likely a result of both categories being still far from the idealized computational model.

C.4.6 Faradaic efficiency results

Instead of fitting on production rates, we can also try fitting on the Faradaic efficiencies of the different products . Results for the CO_2RR products are shown in Figure 22. Overall, results on LOO are on par and some instances better (CO - 0.55 vs. 0.44) than those trained for production rate. However, the same is not true for LOCO, where results are mixed. Both sets of results still suggest a very poor correlation.

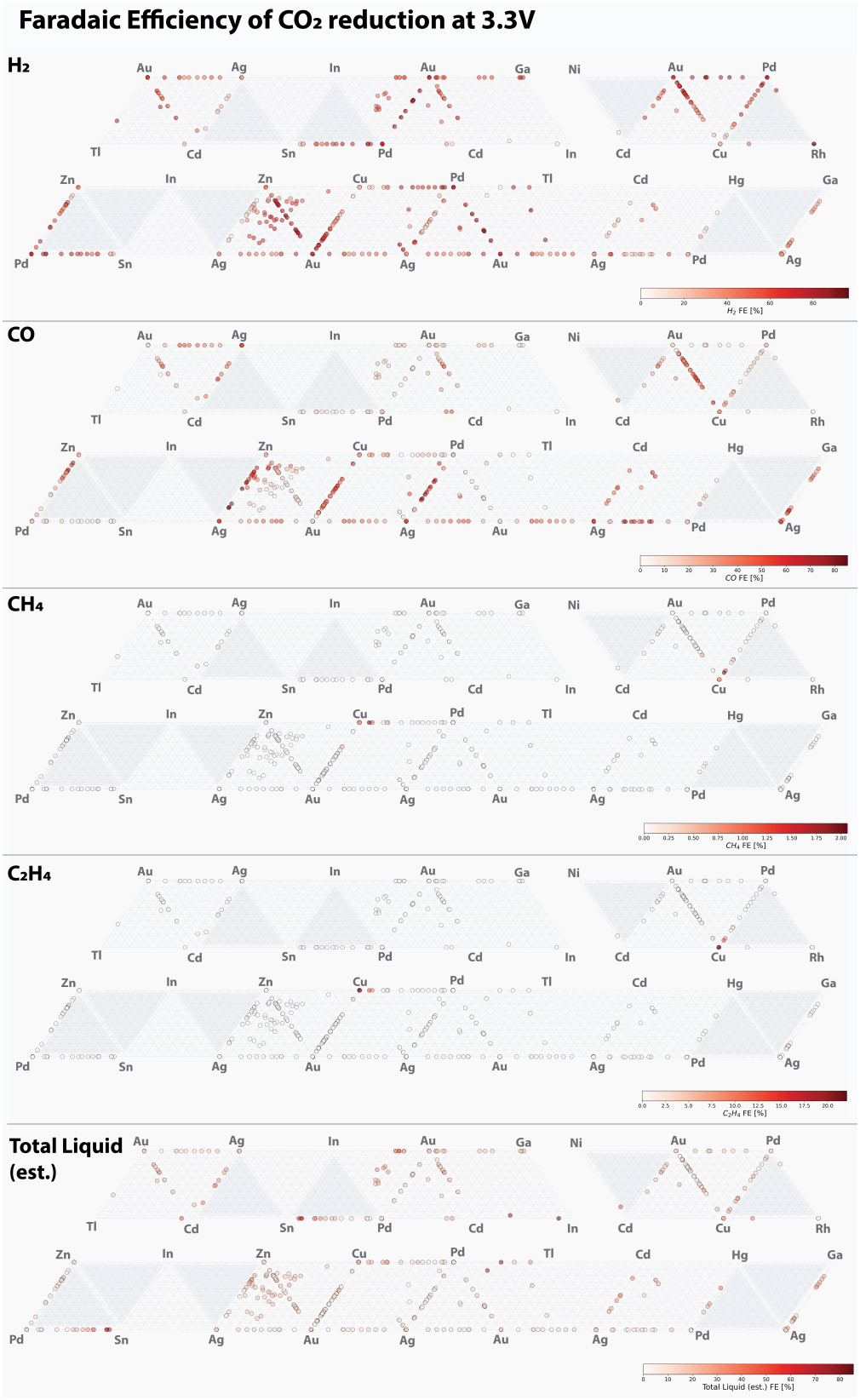

Figure 14 Mapping of Faradaic Efficiency (FE%) for H_2, CO, CH_4, C_2H_4, and estimated Total Liquid onto the XRF composition space. Darker shaded ternary phase diagrams result from connecting several diagrams and were not intentionally explored

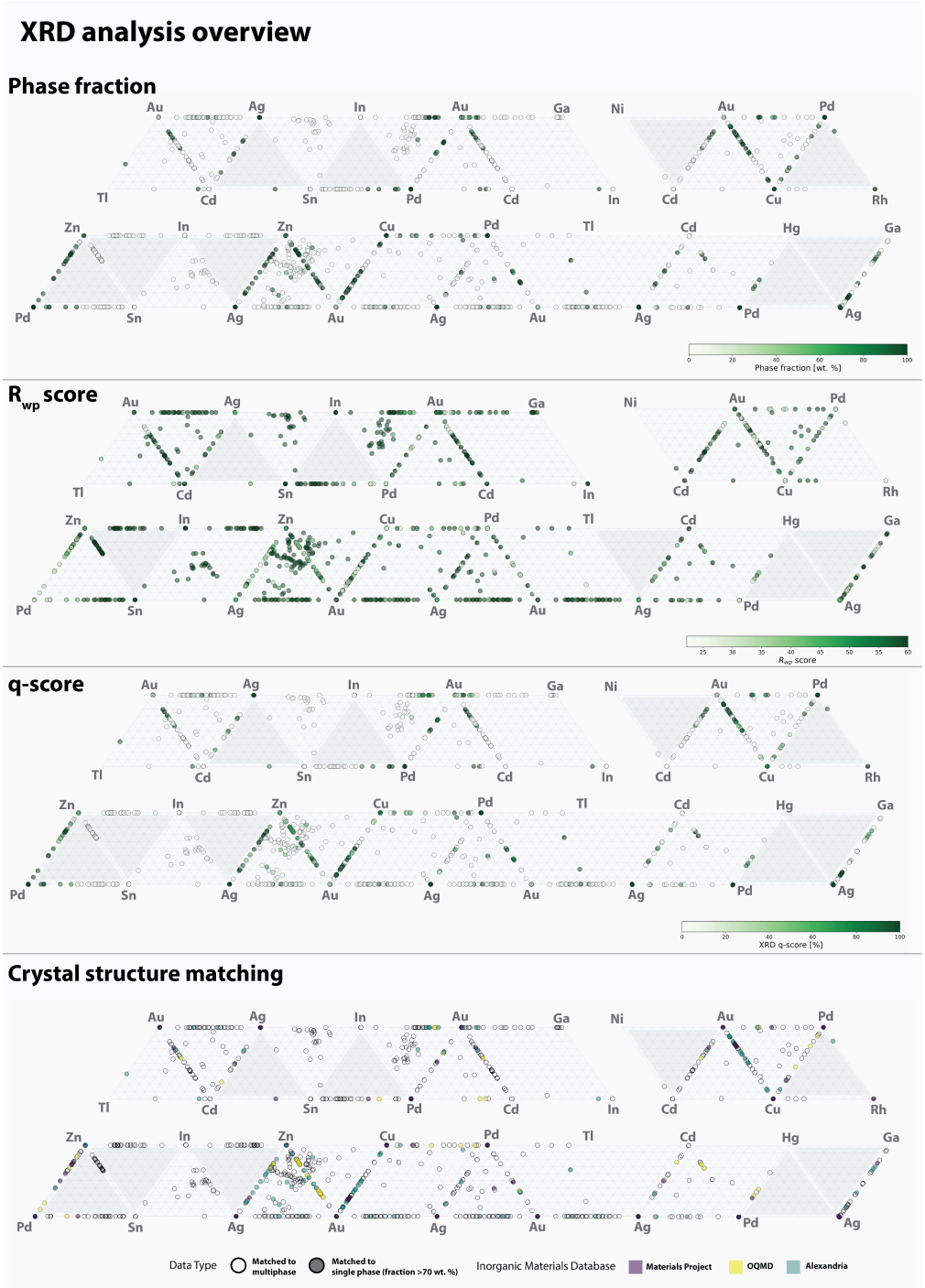

Figure 15 Mapping of XRD analysis results including phase fractions, $R_{wp}score$, $q-score$, and crystal matching indicating cif file source. Darker shaded ternary phase diagrams result from connecting several diagrams and were not intentionally explored

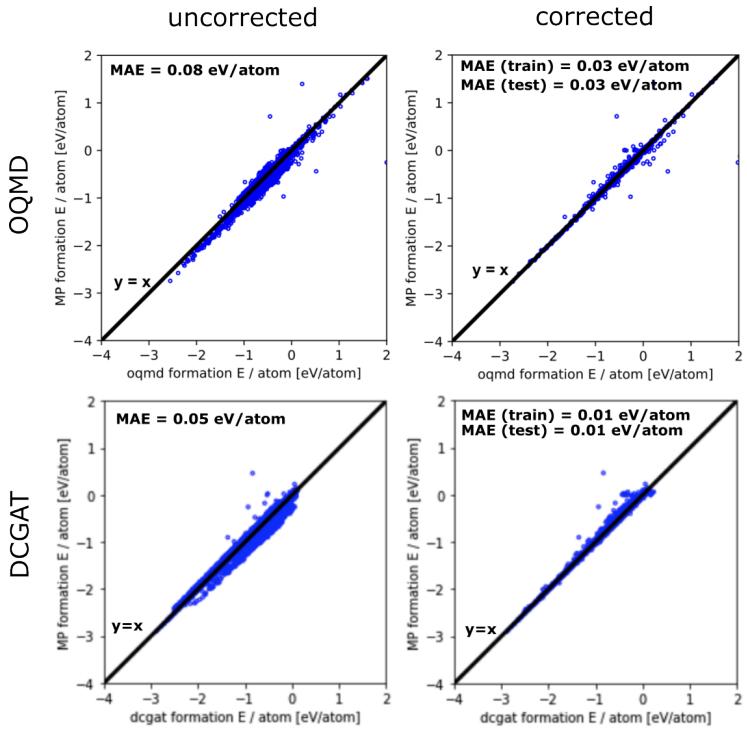

Figure 16 The linear formation energy corrections applied to the materials coming from OQMD and Alexandria (DCGAT) to correct small differences in the pseudopotentials so that comparisons could be made to MP materials for the purposes of assessing Pourbaix stability.

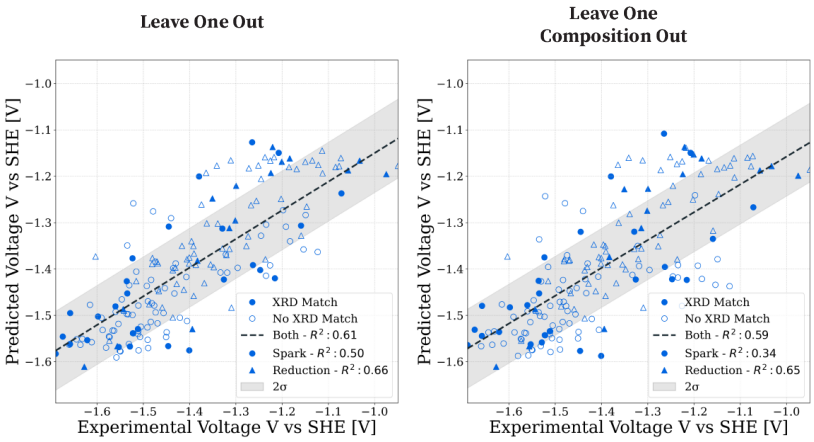

Figure 17 HER predicted voltage for the two different cross-validation strategies. A linear model was used with features coming from mean adsorption energies.

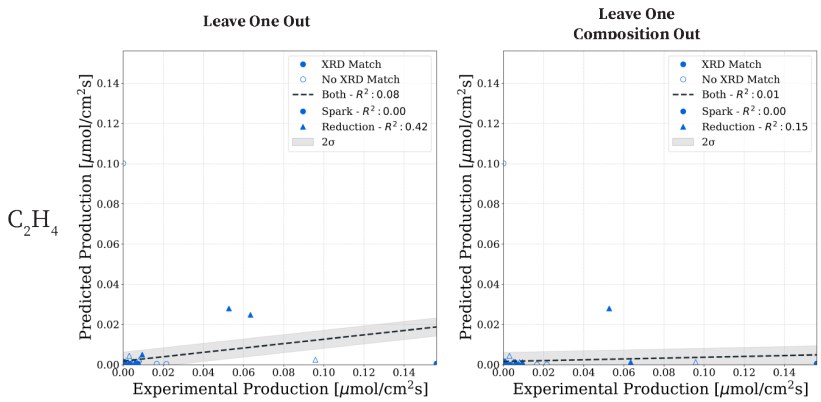

Figure 18 CO_2RR predicted production rates for C_2H_4 under different cross-validation strategies. A random forest regression model was used with features coming from Boltzmann weighted adsorption energies and elemental Matminer features.

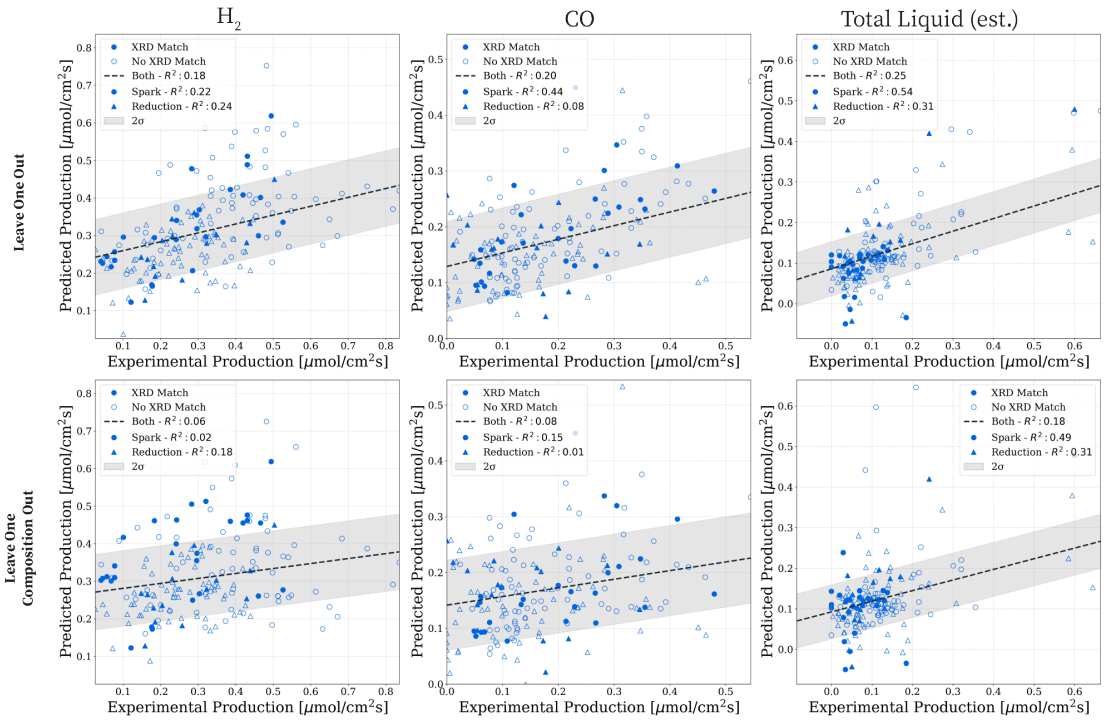

Figure 19 CO_2RR predicted production rates across several products - H_2, CO, and Total Liquid for the two different cross-validation strategies. A **linear model** was used with features coming from Boltzmann weighted adsorption energies and elemental Matminer features.

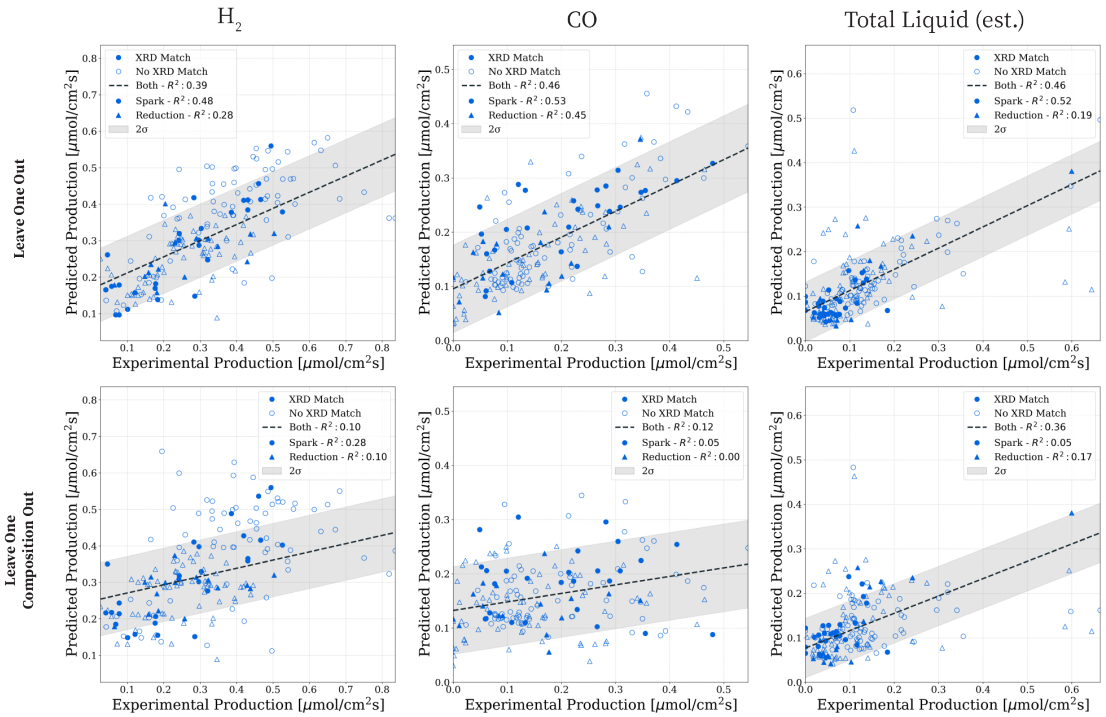

Figure 20 CO_2RR predicted production rates across several products - H_2, CO, and Total Liquid for the two different cross-validation strategies. A random forest regression model was used with **only elemental Matminer features.**

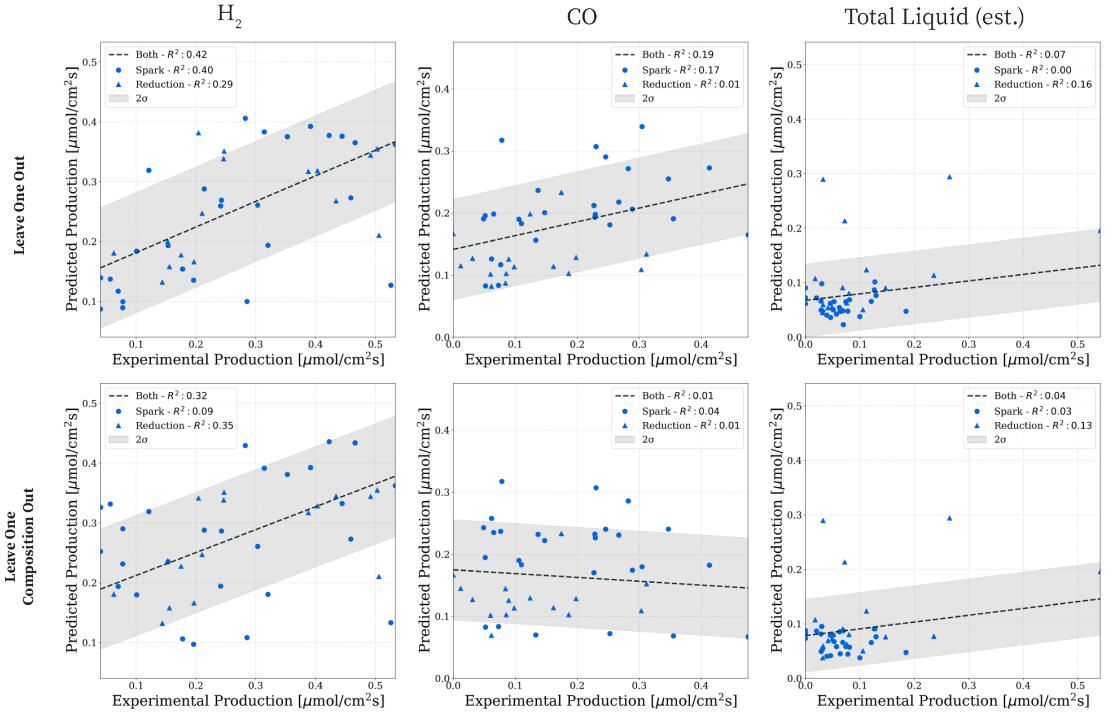

Figure 21 CO_2RR predicted production rates across several products - H_2, CO, and Total Liquid for the two different cross-validation strategies. Only **XRD matched** samples were considered in this analysis.

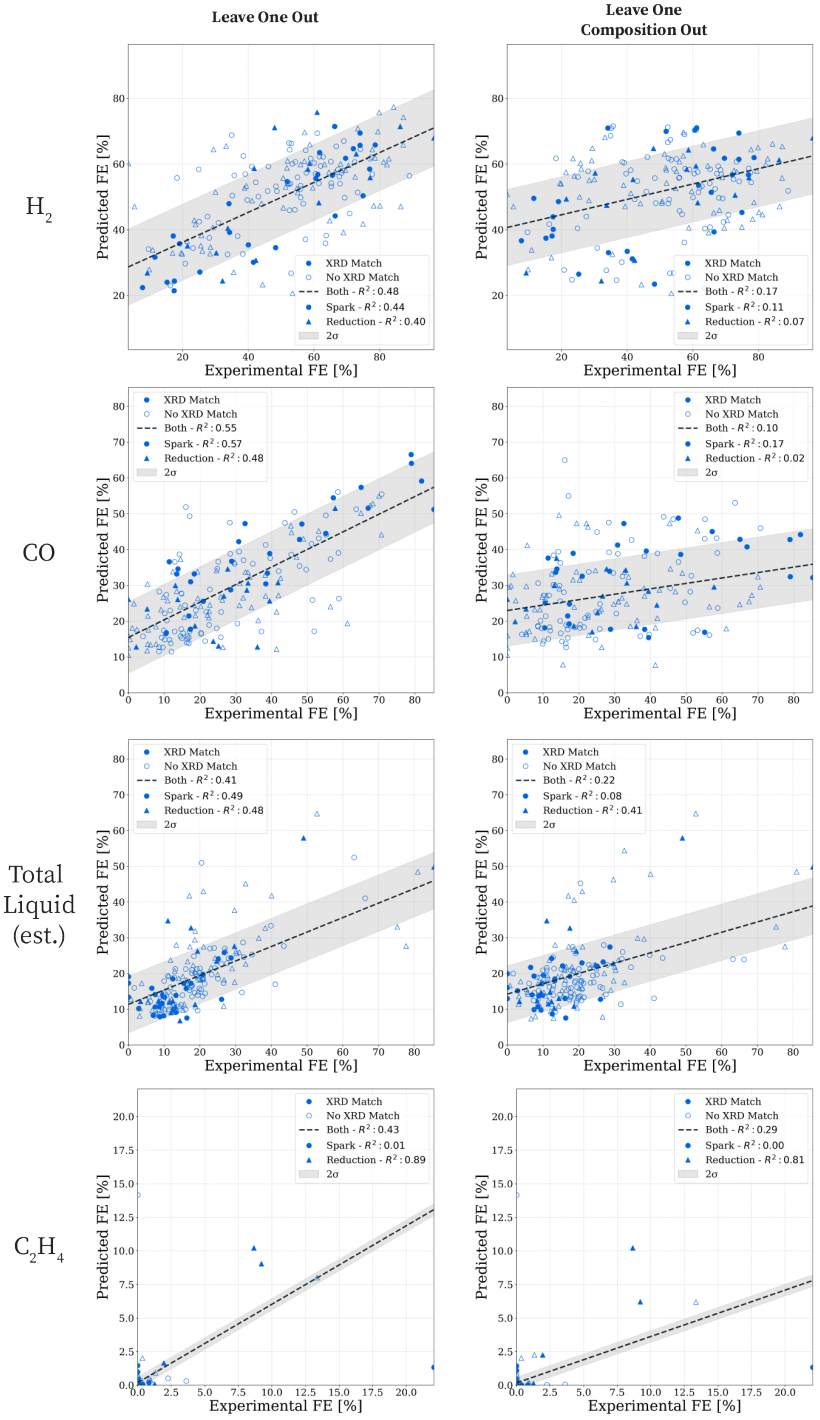

Figure 22 CO_2RR predicted **Faradaic efficiencies** across several products - H_2, CO, Total Liquid, and C_2H_4 for the two different cross-validation strategies. A random forest model was used with features coming from Boltzmann weighted adsorption energies and elemental Matminer features.

C.5 HER Candidates

material id	composition	predicted voltage V v. SHE	material id	composition	predicted voltage V v. SHE
oqmd-1128070	Mo-0.25-Nb-0.25-W-0.5	0.20	dcgat-agm002185003	Se-1.0	-1.17
mp-1187206	Ta-0.75-W-0.25	-0.80	mp-1071078	Ni-0.333-Se-0.667	-1.17
oqmd-447729	Mo-0.5-V-0.25-W-0.25	-0.91	dcgat-agm002183076	Cd-0.5-S-0.5	-1.17
mp-20456	Co-0.429-Se-0.571	-0.92	mp-973053	H-0.75-Sc-0.25	-1.17
oqmd-472683	Ga-0.25-Mn-0.5-Zn-0.25	-0.95	dcgat-agm003184034	Pb-0.25-Se-0.5-Tl-0.25	-1.17
dcgat-agm002153716	Ge-0.111-H-0.889	-0.96	dcgat-agm003062322	Cu-0.25-Se-0.5-Zn-0.25	-1.17
oqmd-520732	Ga-0.5-Mn-0.25-Tc-0.25	-0.98	dcgat-agm003153632	Hg-0.25-Se-0.5-Zn-0.25	-1.17
oqmd-393713	Co-0.25-Mo-0.25-V-0.5	-0.98	mp-580226	Cu-0.5-Se-0.5	-1.17
mp-1030108	Mo-0.083-Te-0.667-W-0.25	-1.00	mp-1063938	As-0.5-Mn-0.5	-1.17
mp-11501	Mn-0.25-Ni-0.75	-1.02	dcgat-agm003144793	Bi-0.4-Se-0.6	-1.17
mp-600124	Mn-0.333-Ni-0.333-Sb-0.333	-1.03	mp-1103177	Fe-0.333-Se-0.667	-1.18
oqmd-1222216	Cu-0.5-Se-0.5	-1.03	dcgat-agm003738920	Sb-0.167-Se-0.667-Sn-0.167	-1.18
dcgat-agm002183072	Cd-0.5-S-0.5	-1.03	oqmd-1555855	Hg-0.5-Se-0.25-Te-0.25	-1.18
dcgat-agm002185503	Hg-0.143-Se-0.571-Tl-0.286	-1.04	mp-22745	Co-0.529-Se-0.471	-1.18
dcgat-agm002185494	Cd-0.143-Se-0.571-Tl-0.286	-1.05	dcgat-agm003204187	Se-0.667-Tl-0.333	-1.18
dcgat-agm003062314	Cu-0.25-Se-0.5-Zn-0.25	-1.05	dcgat-agm003062313	Cu-0.25-Se-0.5-Zn-0.25	-1.18
dcgat-agm002193870	Se-0.571-Tl-0.286-Zn-0.143	-1.06	dcgat-agm002370150	Co-0.167-Se-0.833	-1.18
dcgat-agm002184996	Se-1.0	-1.06	mp-1821	Se-0.667-W-0.333	-1.18
dcgat-agm002019659	Se-1.0	-1.06	dcgat-agm003659759	Sb-0.1-Se-0.5-Tl-0.4	-1.18
dcgat-agm003201183	Se-0.5-Tl-0.5	-1.08	mp-1226897	Cd-0.4-Hg-0.1-Se-0.5	-1.18
dcgat-agm002019668	Se-1.0	-1.08	dcgat-agm003198330	Ni-0.167-Se-0.833	-1.18
dcgat-agm003224862	Ge-0.2-H-0.8	-1.08	dcgat-agm002071817	H-0.667-Sb-0.333	-1.18
oqmd-1441866	Cu-0.5-Se-0.5	-1.08	mp-1226039	Co-0.167-Ni-0.167-Te-0.667	-1.18
dcgat-agm002069646	As-0.333-H-0.667	-1.08	mp-1226036	As-0.333-Co-0.333-Se-0.333	-1.18
dcgat-agm003198763	Se-0.667-Tl-0.333	-1.08	dcgat-agm003218501	Se-0.375-Tl-0.625	-1.18
mp-820	Hg-0.5-Se-0.5	-1.09	dcgat-agm003313875	Se-0.556-Te-0.222-Tl-0.222	-1.18
dcgat-agm003143322	Cd-0.25-Hg-0.25-Se-0.5	-1.10	dcgat-agm003143331	Cd-0.25-Hg-0.25-Se-0.5	-1.18
dcgat-agm002185495	Cd-0.143-Se-0.571-Tl-0.286	-1.10	dcgat-agm002018208	Se-0.667-Te-0.333	-1.18
dcgat-agm002183071	Cd-0.5-S-0.5	-1.10	dcgat-agm003765687	Co-0.125-Cu-0.125-Se-0.75	-1.18
dcgat-agm003143326	Cd-0.25-Hg-0.25-Se-0.5	-1.10	dcgat-agm002239472	In-0.4-Se-0.6	-1.19
oqmd-1754148	Cu-0.5-Se-0.5	-1.10	dcgat-agm001623308	Cu-0.2-H-0.2-Mn-0.2-Ni-0.4	-1.19
mp-680646	Ni-0.5-Sn-0.5	-1.10	dcgat-agm002494639	Co-0.2-H-0.6-Nb-0.2	-1.19
mp-673255	Cu-0.529-Se-0.471	-1.10	dcgat-agm003596580	Se-0.444-Te-0.111-Tl-0.444	-1.19
mp-866134	Fe-0.75-V-0.25	-1.11	mp-1223932	Hg-0.5-Se-0.25-Te-0.25	-1.19
oqmd-1105090	Se-0.5-Tl-0.5	-1.11	dcgat-agm002017918	Bi-0.333-Se-0.667	-1.19
mp-1025649	Mo-0.222-Te-0.667-W-0.111	-1.11	dcgat-agm003625178	Cd-0.25-Hg-0.25-Se-0.5	-1.19
oqmd-297717	Co-0.75-Ni-0.25	-1.11	dcgat-agm002018271	In-0.25-Se-0.75	-1.19
dcgat-agm003292803	Se-0.455-Tl-0.545	-1.11	oqmd-20460	As-0.333-Mn-0.333-Ni-0.333	-1.19
dcgat-agm002268684	Cu-0.333-Se-0.667	-1.12	oqmd-7853	Cu-0.4-Se-0.4-Tl-0.2	-1.19
dcgat-agm002019672	Se-1.0	-1.12	mp-1225994	Co-0.333-Se-0.333-Te-0.333	-1.19
dcgat-agm002193869	Se-0.571-Tl-0.286-Zn-0.143	-1.12	oqmd-1480903	As-0.333-Bi-0.333-Sb-0.333	-1.19
dcgat-agm002888614	Cd-0.25-Hg-0.25-Se-0.5	-1.12	oqmd-1739776	Mo-0.333-Se-0.667	-1.19
dcgat-agm003061770	Cu-0.25-Hg-0.25-Se-0.5	-1.12	dcgat-agm003193011	Se-0.5-Te-0.25-Tl-0.25	-1.19
dcgat-agm002183073	Cd-0.5-S-0.5	-1.12	dcgat-agm002295867	Ni-0.333-Se-0.667	-1.19
oqmd-322981	Mn-0.25-Ni-0.75	-1.12	mp-672	Cd-0.5-S-0.5	-1.19
dcgat-agm003556772	In-0.125-Se-0.5-Tl-0.375	-1.12	mp-1027580	Mo-0.333-S-0.333-Se-0.333	-1.19
oqmd-1368161	Cu-0.333-Se-0.5-Tl-0.167	-1.12	dcgat-agm003676550	Pb-0.417-Se-0.5-Tl-0.083	-1.19
dcgat-agm003212411	Se-0.667-Tl-0.333	-1.12	dcgat-agm003556315	Cd-0.5-S-0.375-Se-0.125	-1.19
mp-1026351	Mo-0.111-Te-0.667-W-0.222	-1.12	dcgat-agm003192331	Hg-0.25-Se-0.5-Te-0.25	-1.19
mp-1226731	Cd-0.1-Hg-0.4-Se-0.5	-1.12	mp-1212695	Ga-0.133-Hg-0.333-Se-0.533	-1.19
mp-1836	Se-0.5-Tl-0.5	-1.13	mp-1025906	Mo-0.333-S-0.222-Se-0.444	-1.19
mp-1025819	Mo-0.333-S-0.222-Se-0.444	-1.13	dcgat-agm002018209	Se-0.667-Te-0.333	-1.19
dcgat-agm003556575	Cu-0.375-Ni-0.125-Se-0.5	-1.13	oqmd-717228	Cu-0.5-Ni-0.25-Zn-0.25	-1.20
mp-14090	Cu-0.25-Se-0.5-Tl-0.25	-1.13	mp-1201566	As-0.125-Se-0.5-Tl-0.375	-1.20
mp-2280	Cu-0.333-Se-0.667	-1.13	mp-20901	Ni-0.333-Se-0.667	-1.20
mp-2000	Cu-0.333-Se-0.667	-1.13	dcgat-agm003062327	Cu-0.25-Se-0.5-Zn-0.25	-1.20
dcgat-agm002069645	As-0.333-H-0.667	-1.13	mp-1065751	Co-0.5-Fe-0.25-Si-0.25	-1.20
dcgat-agm003203021	Se-1.0	-1.13	oqmd-552445	Sn-0.25-Ta-0.25-Tc-0.5	-1.20
dcgat-agm003293190	Se-0.417-Tl-0.583	-1.13	oqmd-1440299	Ni-0.333-Se-0.667	-1.20
dcgat-agm002183074	Cd-0.5-S-0.5	-1.14	dcgat-agm002152745	Bi-0.333-Ge-0.083-Se-0.583	-1.20
dcgat-agm003267594	H-0.889-Si-0.111	-1.14	mp-4492	Co-0.5-Mn-0.25-Si-0.25	-1.20
dcgat-agm001215469	Ge-0.25-Mn-0.25-Ni-0.5	-1.14	mp-1212307	In-0.7-Ni-0.3	-1.20
oqmd-308096	Mo-0.25-W-0.75	-1.14	dcgat-agm002167041	As-0.333-Ni-0.667	-1.20
dcgat-agm003676549	Sb-0.083-Se-0.5-Tl-0.417	-1.14	dcgat-agm002151080	Ga-0.4-Se-0.6	-1.20
oqmd-1473251	Hg-0.5-Se-0.5	-1.14	dcgat-agm002153596	Fe-0.111-H-0.667-Zn-0.222	-1.20
dcgat-agm003183055	Mn-0.25-Ni-0.5-Zn-0.25	-1.14	dcgat-agm003153634	Hg-0.25-Se-0.5-Zn-0.25	-1.20
dcgat-agm002018195	Se-0.667-Te-0.333	-1.14	mp-9814	Cu-0.375-Sb-0.125-Se-0.5	-1.20
dcgat-agm003659717	Se-0.5-Te-0.1-Tl-0.4	-1.14	oqmd-1741060	Bi-0.125-Cu-0.375-Se-0.5	-1.20
dcgat-agm003289670	Se-0.429-Tl-0.571	-1.15	mp-5396	Co-0.5-Mn-0.25-Sb-0.25	-1.20
dcgat-agm002018216	Se-0.667-Te-0.333	-1.15	mp-2090	Co-0.5-Fe-0.5	-1.20
oqmd-1369425	Mn-0.333-V-0.667	-1.15	mp-10074	Ge-0.333-Se-0.667	-1.20
mp-1080603	Co-0.125-Fe-0.875	-1.15	dcgat-agm002018272	In-0.25-Se-0.75	-1.21
dcgat-agm002184995	Se-1.0	-1.15	dcgat-agm003414366	Se-0.5-Te-0.167-Tl-0.333	-1.21
dcgat-agm002018198	Se-0.667-Te-0.333	-1.15	mp-2578	Ni-0.333-Te-0.667	-1.21
oqmd-1752850	Sb-0.125-Se-0.5-Tl-0.375	-1.15	dcgat-agm003615401	Cu-0.5-Se-0.25-Te-0.25	-1.21
dcgat-agm003153628	Hg-0.25-Se-0.5-Zn-0.25	-1.15	dcgat-agm003257709	Cu-0.143-Ga-0.143-Se-0.571-Sn-0.143	-1.21
mp-982261	Pb-0.333-Se-0.667	-1.15	mp-675626	As-0.125-Cu-0.375-Se-0.5	-1.21
mp-22309	Co-0.333-Se-0.667	-1.15	mp-22300	Co-0.5-Fe-0.25-Ge-0.25	-1.21
mp-1226729	Cd-0.25-Hg-0.25-Se-0.5	-1.15	dcgat-agm002264007	Co-0.125-Ni-0.375-Se-0.5	-1.21
mp-568380	Se-0.375-Tl-0.625	-1.15	mp-1226990	Cd-0.273-In-0.182-Se-0.545	-1.21
dcgat-agm003354875	Se-0.615-Te-0.231-Tl-0.154	-1.16	dcgat-agm002018213	Se-0.667-Te-0.333	-1.21
dcgat-agm003676192	Se-0.5-Sn-0.083-Tl-0.417	-1.16	oqmd-1735308	Sb-0.125-Se-0.5-Tl-0.375	-1.21
oqmd-551623	Ga-0.25-Ta-0.25-Tc-0.5	-1.16	oqmd-1473593	Se-0.667-Te-0.333	-1.21
dcgat-agm003455149	Hg-0.143-Se-0.571-Tl-0.286	-1.16	oqmd-1339137	Ga-0.857-Mn-0.143	-1.21
dcgat-agm002144077	Co-0.273-Se-0.727	-1.16	oqmd-1473632	Te-0.667-W-0.333	-1.21
dcgat-agm002345642	Mn-0.167-Se-0.833	-1.16	mp-568661	Cd-0.143-In-0.286-Se-0.571	-1.21
mp-1018722	Hg-0.5-Se-0.5	-1.16	oqmd-1440294	Se-0.667-Te-0.333	-1.21
mp-2469	Cd-0.5-S-0.5	-1.16	dcgat-agm003194428	As-0.4-Se-0.6	-1.21
dcgat-agm003556778	Bi-0.125-Se-0.5-Tl-0.375	-1.16	mp-20862	Co-0.333-Se-0.667	-1.21
dcgat-agm003429338	Pb-0.333-Se-0.5-Tl-0.167	-1.16	mp-2730	Hg-0.5-Te-0.5	-1.21
dcgat-agm003654045	Pb-0.1-Se-0.4-Tl-0.5	-1.16	oqmd-1017516	Co-0.5-Fe-0.25-Ge-0.25	-1.21
mp-601833	Fe-0.812-Ge-0.188	-1.17	mp-1224765	Fe-0.25-Ni-0.083-Sb-0.667	-1.21
dcgat-agm002185433	Se-0.6-Sn-0.4	-1.17	dcgat-agm002018194	Se-0.667-Te-0.333	-1.22
dcgat-agm002018273	In-0.25-Se-0.75	-1.17	oqmd-1739029	Mo-0.333-Se-0.667	-1.22
mp-1026916	Mo-0.333-S-0.333-Se-0.333	-1.17	mp-31406	Bi-0.4-Se-0.4-Te-0.2	-1.22
dcgat-agm002183075	Cd-0.5-S-0.5	-1.17	oqmd-1474575	Sb-0.125-Se-0.5-Tl-0.375	-1.22
dcgat-agm003143324	Cd-0.25-Hg-0.25-Se-0.5	-1.17	mp-1025588	S-0.222-Se-0.444-W-0.333	-1.22
dcgat-agm002381699	Pb-0.25-Se-0.75	-1.17	mp-22784	In-0.25-Ni-0.75	-1.22
dcgat-agm002146833	Cu-0.333-Se-0.667	-1.17	oqmd-1443229	As-0.125-Cu-0.375-Se-0.5	-1.22
oqmd-1736110	Hg-0.143-In-0.286-Se-0.571	-1.17	dcgat-agm002017915	Bi-0.333-Se-0.667	-1.22